Macromolecular Materials and Engineering
www.mme-journal.de

Mechano-Optical Characterization of Extrusion Flow Instabilities in Styrene-Butadiene Rubbers: Investigating the Influence of Molecular Properties and Die Geometry

*Christos K. Georgantopoulos, Masood K. Esfahani, Carlo Botha, Ingo F. C. Naue, Nico Dingenouts, Andrea Causa, Roland Kádár, and Manfred Wilhelm**

The extrusion flow instabilities of two commercial styrene-butadiene rubbers are investigated as they vary in isomer content (1,4-*cis*, 1,4-*trans*, and 1,2 conformation) of the butadiene monomer and the molecular architecture (linear, branched). The investigated samples have similar multimodal molecular weight distribution. Two geometries of extrusion dies, slit and round capillary, are compared in terms of the type and the spatial characteristics of the flow instabilities. The latter are quantified using three methods: a highly pressure sensitive slit die, online and offline optical analysis. The highly pressure-sensitive slit die has three piezoelectric pressure transducers ($\Delta t \approx 10^{-3}$ s and $\Delta p \approx 10^{-5}$ bar) placed along the die length. The characteristic frequency ($f_{Char.}$) of the flow instabilities follows a power law behavior as a function of shear rate to a 0.5 power for both materials, $f_{Char.} \propto \dot{\gamma}_{app.}^{0.5}$. A qualitative model is used to predict the spatial characteristic wavelength (λ) of the flow instabilities from round capillary to slit dies and vice versa. Slip velocities (V_s) are used to quantify the slippage at slit and round capillary dies as well.

1. Introduction

Flow instabilities during polymer extrusion are one of the most crucial challenges for the quality of a product.[1–7] As the extrusion throughput is increased, extrudate can change appearance from a smooth and transparent to matte and afterward to various kinds of surface and/or volume distortions.[5,8–10] Typical names for the flow instabilities, as the shear rate increases, are sharkskin, stick-slip, and gross melt fracture (GMF). Attempting to define these regions, Gansen et al.[11] and Naue et al.[8,9] defined the surface and volume distortions referred to slit die (rectangular cross-section area) geometry. Sharkskin is defined as high frequency ($f_{Char.} \approx 20$ Hz for a specific linear low density polyethylene at 140 °C,[12] and within our study $f_{Char.} \approx 15$ Hz for a specific styrene-butadiene rubber (SBR) at 120 °C) with small amplitude surface distortions. The amplitude of the distortions should be smaller than the thickness of the extrudate for the sharkskin instability. The conventional pressure transducer of a capillary rheometer is not able to capture the high frequency and low amplitude pressure fluctuations during sharkskin instability. Stick-slip instability is characterized by alternating smooth and/or sharkskin regimes as well as irregular distortions at the extrudate surface and volume. It is accompanied by slow pressure (p) fluctuations of $\Delta p/p \approx 25\%$ for $p \approx 200$ bar mean pressure, measured by a conventional pressure transducer in the barrel of a capillary rheometer. GMF is characterized by distortions of the entire extrudate and therefore can be classified as a volume instability. No typical pattern in space and time has been observed for GMF.[10] Gross melt fracture is not further investigated within this presented study.

The influence of die geometry in capillary rheometry has been experimentally and numerically discussed in the literature.[13–20] Experimental studies[15,16] have shown that the onset and the type of flow instabilities are significantly affected by the die geometry even at a similar range of shear rates. For this reason, both slit (rectangular cross-section area) and round capillary (circular cross-section area) dies are used in this investigation. A power law model[3] is used to describe the shear stress dependency as a function of shear rate, followed by

C. K. Georgantopoulos, Dr. M. K. Esfahani, C. Botha, Dr. I. F. C. Naue, Dr. N. Dingenouts, Prof. M. Wilhelm
Karlsruhe Institute of Technology (KIT)
Institute of Chemical Technology and Polymer Chemistry (ITCP)
Engesserstraße 18, Karlsruhe 76131, Germany
E-mail: manfred.wilhelm@kit.edu

Dr. A. Causa
Pirelli Tyre S. p. A., R&D
Viale Piero e Alberto Pirelli 25
Milan 20126, Italy

Prof. R. Kádár
Department of Industrial and Materials Science
Division of Engineering Materials
Chalmers University of Technology
Gothenburg SE-412 96, Sweden

The ORCID identification number(s) for the author(s) of this article can be found under https://doi.org/10.1002/mame.202000801.

DOI: 10.1002/mame.202000801

implementation into the volumetric flow rate equation as suggested by Mooney.[3,23] Consequently, analytical equations for the slip velocity are obtained and used to quantify the slippage at both die geometries (slit and round capillary).[3]

In the last 15 years, an online highly pressure-sensitive in situ mechanical detection slit die has been developed to characterize the flow instabilities during extrusion.[10,11,13,14,22–28] This system was designed for coupling to both capillary rheometers and lab size extruders.[8,9] This slit die is equipped with three highly sensitive piezoelectric pressure transducers (Tr) along the die. These transducers are able to detect minor pressure fluctuations ($\Delta p \approx 10^{-5}$ bar) which appear at the onset of the flow instabilities, and they are associated with the distortions at the extrudate surface.[8,9] During the onset of stick-slip instability an average stick-slip velocity $V_{\text{Stick - slip}}$ needs to be defined. The development of a pressure drop along the slit die during the stick-slip is recorded by the three transducers. Palza et al.[12] suggested to cross-correlate the time-dependent pressure signal of two transducers, thus the cross-correlation time τ_{CC} can be obtained. As the distance between two transducers is known $L^{\text{Tr}_i-\text{Tr}_j}$ the time needed for the stick-slip instability to cross two transducers can be computed by the cross-correlation function (CCF). Hence, the average stick-slip velocity is obtained, $V_{\text{Stick-slip}} = L^{\text{Tr}_i-\text{Tr}_j} / \tau_{CC}$.

Several qualitative models have been used to predict the spatial characteristic wavelength of flow instabilities. Wang et al.,[29] Barone et al.,[30] and Inn et al.[31] have modeled the characteristic sharkskin wavelength for capillary dies. Wang et al.[29] and Barone et al.[30] have studied linear low density polyethylene (LLDPE) samples which exhibit pronounced sharkskin instability. Both studies quantify the spatial characteristic wavelength λ of flow instabilities as $\lambda = V\tau^*$, where V is the average extrudate velocity and τ^* is the characteristic time periodicity. A more complex analytical expression has been proposed by Inn et al.,[31] studying polybutadiene (PBD) samples. They[31] used Cogswell[32] approach to estimate the amount of stretching deformation on the surface of the extrudate at the die exit region. All of those qualitative models[29–31] have been developed based on visual observations of extrudates immediately after the die exit.

In the present study, two commercial styrene-butadiene random copolymers with similar multimodal MWD, chemical composition but different isomer content (1,4-*cis*, 1,4-*trans*, and 1,2 conformation) of the butadiene monomer and different molecular architecture (linear, branched) are investigated. The difference in isomer content of butadiene and molecular architecture of the two samples is related to different types of flow instabilities. Additionally, size-exclusion chromatography (SEC), ^{1}H-nuclear magnetic resonance (NMR), differential scanning calorimetry (DSC), and a newly developed low field SEC-NMR coupling have been performed to gain insight into the molecular properties of the two SBR samples. Thereafter, the samples were extruded through the described highly pressure-sensitive slit die with length of $L = 30$ mm and a rectangular cross-section area of 0.5×5 mm^2 ($H \times W$), and a series of three round capillary dies with aspect ratio of $L/D = 5$, 10, 15 with diameter of $D = 2$ mm coupled to a Göttfert RG 50 capillary rheometer. The extrudate characteristics, such as the spatial wavelength and the characteristic time periodicity (or frequency), have been analyzed using the pressure fluctuations provided by the highly pressure-sensitive slit die. In addition, offline and online optical analyses for both die geometries were performed.[8,9,26,28] First, the time characteristic frequency (or periodicity) was obtained by Fourier transform (FT) analysis of the in situ mechanical pressure fluctuations. Second, transmission polarization microscopy and incident light microscopy were used to quantify the spatial characteristic wavelength λ of the instabilities on the extrudate surface and according to $\lambda = V\tau^*$, the instability characteristic time peridicity τ^* is obtained. Third, an online optical analysis method is presented based on the space–time diagram[26,33–35] capable to obtain the characteristic time periodicity without using estimated values such as the average extrudate velocity. Finally, those three differently obtained periodicities are compared to each other. Additionally, this work modifies the proposed model for the spatial characteristic wavelength λ as discussed by Wang et al.[29] and Barone et al.[30] and makes it capable to predict the wavelength for slit dies as well. Thus, this qualitative model allows us to predict the characteristic wavelength λ of flow instabilities changing from capillary to slit dies and vice versa.

2. Experimental Section

Two commercial SBR, named SBR A and SBR B, were investigated in this study. The samples were characterized using SEC and high field NMR spectroscopy (400 MHz, 9.4 Tesla, ^{1}H). The glass-transition temperature T_g of the samples was investigated via DSC.

To determine the relative molecular weight distribution (MWD) of the SBRs, the SEC was calibrated with polystyrene standards. The elution volume multimode distributions of the two samples are presented in **Figure 1**. The distributions displayed that the two samples have similar elution volume distributions.

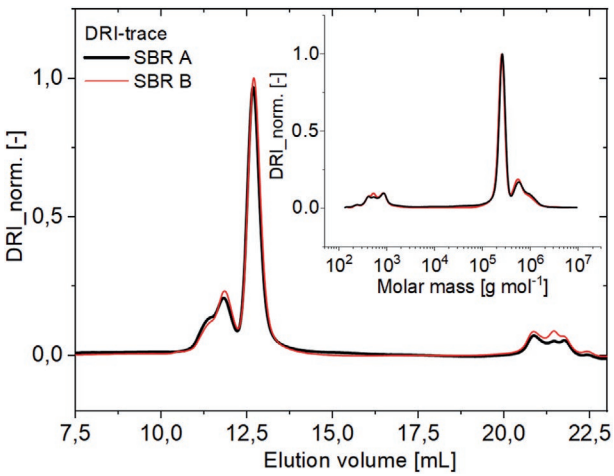

Figure 1. Normalized differential refractive index (DRI) detector response as a function of the elution volume for both SBR samples as obtained by SEC. The inset is the molecular weight distribution (MWD) of both samples. This SEC is equipped with an analytical column with length of 300 mm and inner diameter of 8 mm.

Table 1. Molecular weight characteristics of the two investigated SBR samples.

Name	Elution volume [mL]	Weight percent [wt%]	M_n [kg mol^{-1}]	M_w [kg mol^{-1}]	$Đ$
SBR A	10.0–15.0		286	391	1.36
High MW[b)]	10.0–12.5	26.6	688	757	1.10
Medium MW[b)]	12.5–15.0	68.4	258	260	1.02
Low MW[a)]	20.0–22.5	5.0	0.46	0.65	1.40
SBR B	10.0–15.0		287	390	1.35
High MW[b)]	10.0–12.5	26.0	610	650	1.05
Medium MW[b)]	12.5–15.0	68.0	252	256	1.01
Low MW[a)]	20.0–22.5	6.0	0.42	0.60	1.42

[a)]The weight percent is calculated by the DRI detector as a function of elution volume assuming that the two peaks have similar chemical composition; [b)]The weight percent is calculated from the 2D SEC-NMR data presented in Figure 6.

The molecular weight component, presented at elution volume between 10 and 15 mL, has a bimodal distribution with a distinct separation point of the two modes at about ≈12.5 mL. Moreover, substantially low molecular weight fractions have also been identified within the investigated samples between an elution volume of 20 and 22.5 mL.

For the bimodal fraction (elution volume of 10–15 mL), the relative weight compositions of the two modes are similar as well (**Table 1**). The weight average molecular weights M_w of the respective components differ by a factor of 3 and almost 2.5 for SBR A and B, respectively (Table 1). Besides, the overall M_w values are similar for both of them, 390 kg mol^{-1}. The overall M_n values and the M_n values of the medium molecular weight component for the investigated samples are similar as well ≈290 and ≈255 kg mol^{-1}, respectively (Table 1). The low molecular weight component (elution volume 20–22.5 mL) has similar estimated value for the weight average molecular weight of $M_w \approx 0.62$ kg mol^{-1} for both samples.

In Section 5, the investigated samples are characterized by a new combined method using a low field benchtop NMR (62 MHz, 1.45 Tesla, ^{1}H) spectrometer coupled to SEC.[36] This technique was used to characterize the chemical composition of the different molecular weight components within the investigated samples. From the results obtained by SEC-NMR, the low molecular weight fraction listed in Table 1 (Low MW) is identified as a low molecular weight hydrocarbon species.

Moreover, high field NMR spectroscopy (400 MHz, 9.4 Tesla, ^{1}H) was used to determine the chemical composition and the relative isomer content of the butadiene monomer for the SBRs (**Table 2**). In rubber science, the isomer of the 1,2 butadiene is typically referred to as vinyl.[43] The isomer distribution of the butadiene is important for several reasons.[43] First, it modifies the glass-transition temperature T_g of SBR, and second, it has been shown[44] that SBR with a high 1,4-*cis*-polybutadiene conformation has significantly improved abrasion and tear resistance.

One of the most important properties of any elastomer is its glass-transition temperature, T_g. As discussed previously, T_g is controlled in SBRs by adjusting the monomer ratio of styrene to butadiene and the isomer of the butadiene units as well.[43] DSC characterization was used to investigate the T_g of the SBR samples (Table 2). Each of the samples has only one glass transition temperature, thus phase separation is not detectable at a large length scale (i.e., $l > 3$–5 nm) in these two systems.

The capillary extrusion temperature was chosen similar to typical industrial processing conditions[43] for SBR polymers, that is, 120 °C for both of the samples. Owing to the appearance of different types of flow instabilities, where SBR A displays sharkskin and SBR B displays sharkskin and stick-slip, SBR A was tested at 145 °C as well. Thus, it was studied under the same temperature difference from the T_g (Table 2) as the SBR B. However, at 145 °C the SBR A did not present stick-slip instability in the entire range of the investigated apparent shear rates, from $\dot{\gamma}_{app.} = 10^0$–$10^3$ s^{-1}. The temperature difference with respect to T_g at 120 °C is 156.3 °C for the SBR A and 180.7 °C for the SBR B. It is known[47] that more than 100 °C above the T_g, the effect of the butadiene isomer is neglectable compared to the influence of topological constraints (entanglements) and molecular architecture (i.e., branching).

Table 2. Chemical composition in weight percentage (wt%) and the glass-transition temperature of the two investigated SBR samples obtained by high field NMR and DSC, respectively.

Name	Styrene [wt%]	Butadiene 1.2 [wt%]	Butadiene 1,4 (*cis* and *trans*) [wt%]	T_g[a)] [°C]
SBR A	23.5	47.3	29.2	−36.3
SBR B	16.3	25.2	58.5	−60.7

[a)]The heating/cooling rate was 5 K min^{-1} with a temperature range of −90 and 160 °C. The second heating run was analyzed.

3. Characterization Techniques

In this section, techniques which have been used and developed to characterize the flow and the process behavior of the investigated samples are presented.

3.1. Oscillatory and Extensional Rheology

Rheological experiments were carried out in the linear and nonlinear regime using a TA Instruments ARES-G2

(New Castle, DE) strain-controlled rheometer. For the oscillatory frequency sweep experiments, the rheometer is equipped with a grooved plate-plate geometry, with a diameter of 8 mm to reduce slippage. The SBR samples were tested by an isothermal time sweep which has been performed at 120 °C, $\omega/2\pi = 1$ Hz and strain amplitude of $\gamma_0 = 3\%$. The storage modulus G' stayed constant within 5% at 110 kPa for more than 2 h which confirms the thermal stability of the samples. Small amplitude oscillatory shear (SAOS) frequency sweep tests were performed within $\gamma_0 = 1$–3% strain amplitude in the linear viscoelastic (LVE) regime to obtain the magnitude of the complex viscosity, storage and loss moduli in a wide range of temperatures from −45 to +120 °C. Moreover, the nonlinear rheological behavior of the samples was investigated by uniaxial extensional rheology. The extensional viscosity fixture (EVF) was coupled to the ARES-G2 rheometer, and the transient extensional viscosity of the samples was determined at 120 °C.

3.2. Capillary Rheology

Capillary rheology of the samples was studied using a Göttfert RG 50 capillary rheometer (Buchen, Germany) equipped with a home-built highly pressure-sensitive slit die system, including a series of conventional round capillary dies as well. The slit die comprises a series of three highly pressure-sensitive piezoelectric (Kistler 6182CA) pressure transducers (Tr) distributed along the slit die. Each transducer is located, at (Tr1) 5 mm, (Tr2) 15 mm, and (Tr3) 25 mm from the die entrance (**Figure 2**). Two types of extrusion dies were compared in this study: a slit (rectangular cross-section area) die and round capillary (circular cross-section area) dies. The extrusion slit die has a rectangular cross-section of width, $W = 5$ mm and height, $H = 0.5$ mm, over a length of $L = 30$ mm. Consequently, the aspect ratios

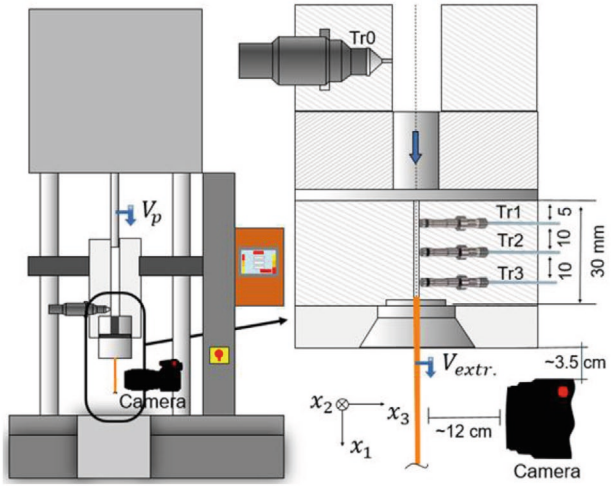

Figure 2. Schematic representation of the capillary rheometer and the highly pressure sensitive slit die. Marked transducers: Tr0 – conventional pressure transducer, Tr1 – Tr3 – Kistler (6182CA) highly sensitive piezoelectric pressure transducers. The ex situ online optical visualization system (camera) is placed at a distance of ≈3.5 cm below the die exit and ≈12 cm from the extrudate surface. The x_2 is the direction of the width (W), and the x_3 is the direction of the height (H).

are $W/H = 10$ and $L/H = 60$. The three round capillary dies have diameter of $D = 2$ mm and aspect ratios of $L/D = 5$, 10, 15. In the highly pressure-sensitive slit die, the sensing element (piezoelectric transducers) diameter is 2.5 mm and provides the in situ detection of the mechanical pressure fluctuations. The piezoelectric transducer system provides time and pressure resolutions, of $\Delta t \approx 10^{-3}$ s and $\Delta p \approx 10^{-5}$ bar up to nominal pressure of $p = 2000$ bar.[24] The mechanical time-dependent pressure signal from the three piezoelectric pressure transducers is subjected to oversampling (online; sampling rate of 400 data points s^{-1}) to improve the signal-to-noise ratio (S/N) and acting as a low pass filter as well.[37] Afterward, it is baseline corrected with a first-order polynomial fit function to eliminate the signal drift and random noise and fitted with an autocorrelation function.[8] Furthermore, the data are then apodized with an exponential function and zero filled with double the amount of data points prior to Fourier transformation (FT) to increase the signal-to-noise ratio. The data handling of the raw mechanical time-dependent pressure signal is inspired by NMR spectroscopy data processing technique where usually the signal processing has key importance to improve the sensitivity of the technique and enhance the S/N. More details regarding the experimental system and time data processing can be found elsewhere.[8,9,12,23–25]

3.3. Optical Analysis of Extrudatess

Offline optical analysis of the collected extrudates was carried out by transmission polarized microscopy and incident light microscopy at room temperature. Transmission polarized microscopy is a contrast-enhancing technique allowing to evaluate the surface structure of the extrudate, which uses polarizing filters. The polarizing filters select a single orientation among all waves which composes of the light and drives it through the investigated sample. Incident light microscopy is the method of choice for the imaging of specimens, specifically surfaces that remain opaque even at thickness of 30 µm.

A Keyence VHX 900F (Osaka, Japan) and a Zeiss Axiophot (Oberkochen, Germany) microscopes were used in this study. The Keyence VHX 900F microscope is equipped with two zoom lenses and magnification range between 20 and 2000. The Zeiss Axiophot microscope is equipped with two objectives of 2.5 and 10, and one ocular magnification of ten times, which result in 25 and 100 times optical magnification. Cylindrical-shaped extrudates, obtained by the round capillary die, were studied via the incident light microscopy where high-resolution images are obtained. Rectangular-shaped extrudates, obtained by the slit die, were investigated using the transmission polarized microscope owing to their thin thickness of about ≈0.5 mm.

Assuming a change on the extrudate surface structure after the extrusion, an online optical method is implemented to overcome this problem. The online optical setup consists of a Pentax XP (Tokyo, Japan) camera as an online extrudate optical monitoring system. The camera is positioned ≈3.5 cm below the slit die exit, perpendicular to the extrudate width (front view, x_1–x_2, Figure 2). The lens consists of a Sigma 105 mm DC Macro EX

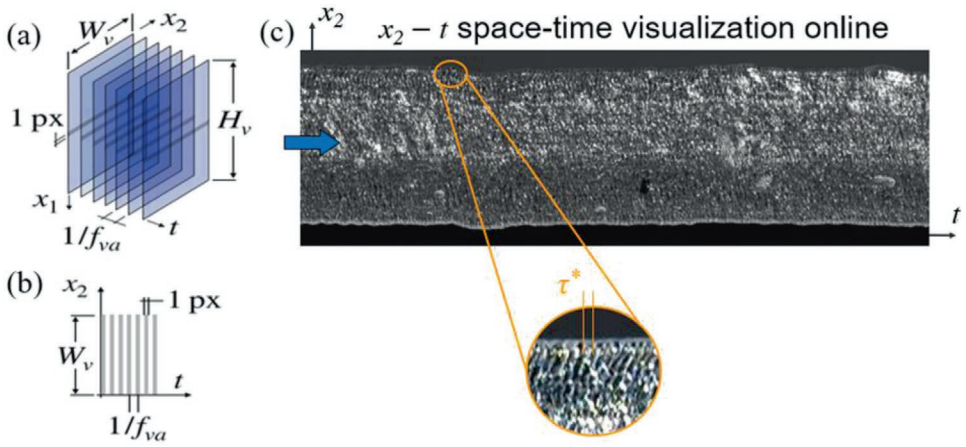

Figure 3. a,b) Illustration of the basic principle for constructing a space-time[26,33–35] visualization from a video with frame dimensions $W_v \times H_v$ and frame (acquisition) rate of f_{va}. c) Example of an online $x_2 - t$ space–time visualization. An enlarged part of the visualization diagram presents the sharkskin stripes and the characteristic time periodicity of them. The investigated sample is SBR A at 120 °C and $\dot{\gamma}_{app} = 7\ s^{-1}$ obtained by the slit die with $H = 0.5$ mm, $W = 5$ mm, and $L = 30$ mm. The blue arrow indicates the extrusion direction.

(Kawasaki, Japan), thus allowing appropriate magnification while positioned at a distance of ≈12 cm from the extrudate. Full high-definition (1960 × 1080 pixels) video recordings at 60 frames per second (fps) were acquired for 5–7 min during extrusion via an online remote acquisition system. Offline and online optical imaging are used to determine the spatial and time characteristics of extrudate patterns as mentioned before.

The basic principle for constructing space–time[26,33–35] visualization from online optical observations is presented and exemplified in **Figure 3**.

The video is recorded with frame dimensions $W_v \times H_v$ and a frame (acquisition) rate of f_{va}. A line of pixels (px) at a fixed position along x_1 can be extracted successively from each frame of the movie (Figure 3a) and added to a newly created image (Figure 3b). Hence, one axis corresponds to the width of the video frame W_v and the other to the experimental time t, with the distance between each line of pixels determined by $1/f_{va}$. An example is shown in Figure 3c for the SBR A sample at 120 °C and $\dot{\gamma}_{app} = 7\ s^{-1}$. The space–time diagram allows an easier extraction of grayscale intensity variations for long data sets and better identification of the characteristic time periodicity τ^* of the flow instability, as it does not use estimated values like the extrudate velocity, explained next.

In **Figure 4**, an example of a stick-slip instability is presented. Figure 4a represents the extrudate obtained by the slit die ($H = 0.5$ mm, $W = 5$ mm, and $L = 30$ mm), which results from one pressure oscillation during stick-slip instability of SBR B at $\dot{\gamma}_{app} = 100\ s^{-1}$ and 120 °C. The first part of the extrudate is sharkskin instability and represents the stick part, that is, the pressure increases for about ≈30 s from $p = 200$ to 250 bar (Figure 4b). The second part has volume and surface distortions not accounted through commonly used nomenclature and represents the slip part, that is, the rapidly decreased pressure for about ≈10 s from 250 to 200 bar (Figure 4b). The slip part presents regular distortions on the side of the extrudate as well, these distortions are characterized by this study as side slide instabilities (Figure 4a). The time duration of the stick-slip instability depends on the shear rate. Typically, as the shear rate is increased, the stick-slip instability happens faster. In Figure 4b, the mechanical pressure fluctuations during stick-slip instability are observed under the same conditions, the shaded area with the four pressure oscillations has been video recorded. The space–time diagram constructed by the recorded video is shown in Figure 4c, where the four stick-slip events are presented. The stick and slip parts are indicated in the space–time diagram as well.

4. Modeling

In this section, the fitting of the steady-state viscosity as a function of wall shear rate, the modeling of the slip velocity, and the characteristics (in time and space) of the flow instabilities are presented. The steady-state viscosity obtained by the capillary rheometer is fitted by the Carreau model[38] (Equation (1)) to quantify the difference between the two samples. Moreover, the shear-thinning regime of the investigated samples obtained by the oscillatory frequency sweeps is fitted by a power law model (Equation (2)). Then, this power law function is included[3] to the volumetric flow rate equation suggested by Mooney[21] (Equation (3)) to obtain analytical equations and predict the slip velocity for both dies geometries (Equations (4) and (5)).[3] Finally, a modified version (Equation (13)) of the model proposed by Wang et al.[29] and Barone et al.[30] is presented for the spatial characteristic wavelength of extrudates obtained by round capillary die, to predict the spatial characteristic wavelength for extrudates obtained by slit die as well.

4.1. Viscosity Models

Using the Cox-Merz rule (explained below) where $\eta(\dot{\gamma}) = |\eta^*(\omega)|$, with the numerical values of $\dot{\gamma} = \omega$ (Figure 8).[50] A Carreau model,[38] Equation (1), is used to fit the steady-state viscosity data from capillary rheometry for each material. In

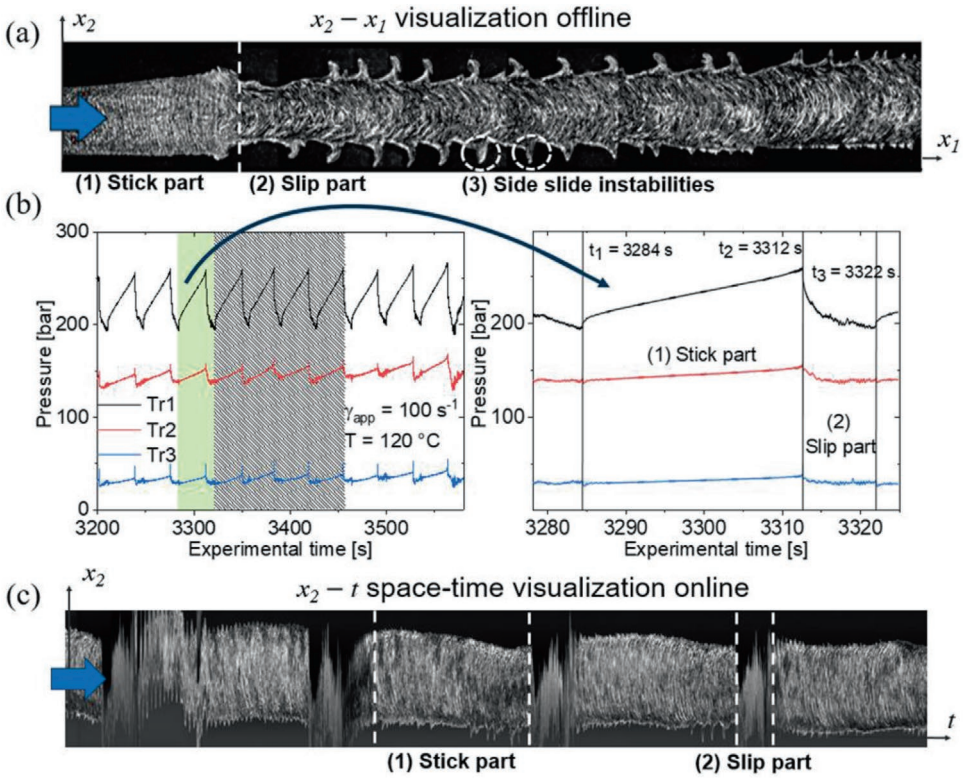

Figure 4. a) Offline optical analysis of an extrudate with stick-slip instability, which represents one pressure oscillation. The first part of the extrudate represents the stick and the second part the slip and the side slide instabilities. b) The greenish area is enlarged at the right-hand figure and indicates the two different time durations and pressure profiles from the stick and slip part. b,c) The gray shaded area represents the pressure signal from the three piezoelectric transducers corresponding to four stick-slip events which have been video recorded, and their space–time[26,33,34,35] diagram is presented. The investigated sample is the SBR B at 120 °C and $\dot{\gamma}_{app}$ = 100 s^{-1} obtained by the slit die with H = 0.5 mm, W = 5 mm, and L = 30 mm. The blue arrows indicate the extrusion direction.

addition, a power law model, Equation (2), fits the shear rate dependent (shear-thinning) magnitude of the complex viscosity data from the rotational rheometer. Thus, K and n are material-dependent parameters and are used for the computation of the slip velocity. The fitting values of the models are listed in **Table 3**

$$\eta(\dot{\gamma}) = \frac{\eta_0}{\left(1+(\tau\dot{\gamma})^2\right)^{\frac{1-m}{2}}} \quad (1)$$

$$\left|\eta^*(\omega)\right| = \eta(\dot{\gamma}) = K\dot{\gamma}^{n-1} \quad (2)$$

where η_0 is the zero shear viscosity, and τ is the longest characteristic relaxation time of the material.

Table 3. Carreau (Equation (1)) and power law (Equation (2)) fitting parameters obtained at 120 °C.

Name	Carreau			Power law	
	m	τ [s]	η_0 [kPa s]	n	K [kPa]
SBR A	0.13	0.35	55	0.17	180
SBR B	0.17	0.90	140	0.19	210

4.2. Slip velocity

Mooney[21] derived the following general formula (Equation (3)) for the volumetric flow rate Q of a round capillary die of radius R and length L. Assuming[21] steady-state conditions, well-developed velocity profile, and an incompressible non-Newtonian flow in the presence of wall slip which is assumed to be solely a function of the wall shear stress[3]

$$Q = \pi R^2 V_s + \frac{\pi R^3}{\sigma_W^3}\int_0^{\sigma_W} \dot{\gamma}\,\sigma_{rz}^2 \mathrm{d}\sigma_{rz} \quad (3)$$

In Equation (3), σ_{rz} is the shear stress and σ_W is the wall shear stress (at radius $r = R$). The first term describes the volumetric flow rate of slippage, and the second term is volumetric flow rate in the absence of slippage (slip velocity, $V_s = 0$). Moreover, the apparent shear rate for the round capillary and slit dies are defined as $\dot{\gamma}_{app.}^{Capillary} = 4Q/\pi R^3$ and $\dot{\gamma}_{app.}^{Slit} = 6Q/WH^2$, respectively, where R is the radius of the round capillary die, W is the width (here W = 5 mm), and H the height (here H = 0.5 mm) of the slit die.

Assuming that the shear-thinning regime of the investigated SBR samples can be simply modeled by a power law behavior (Figure 8), as defined by Equation (2). Then Equation (3) can be integrated and then Rabinowitsch–Weissenberg[4] corrected

to yield the following formulas[3,4] for the slip velocity $V_s^{\text{Capillary}}$ of round capillary die flow

$$V_s^{\text{Capillary}} = \frac{D}{8}\left(\dot{\gamma}_{\text{app}} - \frac{4n}{3n+1}\left[\frac{\sigma_W}{K}\right]^{\frac{1}{n}}\right) \tag{4}$$

and for the slip velocity V_s^{Slit} of slit die flow

$$V_s^{\text{Slit}} = \frac{H}{6}\left(\dot{\gamma}_{\text{app}} - \frac{3n}{2n+1}\left[\frac{\sigma_W}{K}\right]^{\frac{1}{n}}\right) \tag{5}$$

Equations (4) and (5) can be used to determine the slip velocity of molten polymers as a function of the wall shear stress. The extrudate velocity $V_{\text{ext.}}$ is calculated according to a volume flux balance

$$V_{\text{ext.}} = V_{\text{piston}}\frac{A_{\text{barrel}}}{A_{\text{die}}} \tag{6}$$

where A_{barrel} and A_{die} are the cross-sectional areas of the barrel (or reservoir) of the capillary rheometer and the die, respectively. In case of a passive polymer–wall interface (i.e., no chemical interaction between the polymer and solid surface), Brochard-Wyart and de Gennes[39] proposed an interfacial rheological law in terms of an extrapolation length b, as follows

$$V_s = b\left[\frac{dV}{dy}\right]_{y=0} = b\dot{\gamma}_w \tag{7}$$

where V_s is the slip velocity, V is the velocity of the fluid, and $[\frac{dV}{dy}]_{y=0}$ is the shear rate, presented by the Dirichlet boundary condition at $y = 0$, and $\dot{\gamma}_W$ is the wall shear rate.

The custom-built slit die encloses a series of three piezoelectric pressure transducers distributed along the slit die. Palza et al.[12] suggested to study the flow dynamics along the die land with the cross-correlation of the time-dependent pressure signal from the piezoelectric transducers. Thus, the time-dependent cross-correlation can be computed. The maximum is the so-called cross-correlation time and represents the time that an event needs to travel from Tr_i to Tr_j. Hence, in case of stick-slip instability, the average stick-slip velocity $V_{\text{Stick – slip}}$, that is, the average velocity of the stick part and slip part, can be captured by the three transducers during its flow along the die land. The time cross-correlation function is defined by Equation (8)[40]

$$f_{\text{corr}}^{i,j}(\tau) = \frac{\int_0^\infty p_i(t)\,p_j(t+\tau)\,dt}{\int_0^\infty p_i(t)\,p_j(t)\,dt} \tag{8}$$

The subscripts i and j represent different transducers. The time-dependent pressure signal from the piezoelectric pressure transducers is first drift baseline corrected with a first-order polynomial, and the mean pressure value is subtracted, $p(t) = p(t)_{\text{drift corrected}} - p_{\text{mean}}$. Then it is cross-correlated and normalized so the covariance at zero lag are identical 1. For periodic functions, the cross-correlation function is also periodic.[40] If there is a maximum in the cross-correlation function, then it is highly correlated, therefore the events could be assumed to happen simultaneously. The time where the first maximum occurs is the cross-correlation time, τ_{CC}. Using the cross-correlation time, which is the time that one pressure oscillation of the stick-slip instability travels from Tr_i to Tr_j, and the known distance between the transducers $L^{\text{Tr}_i-\text{Tr}_j}$, the $V_{\text{Stick – slip}}$ can be calculated. Thus, $V_{\text{Stick – slip}}$ is obtained by

$$V_{\text{Stick–slip}} = L^{\text{Tr}_i-\text{Tr}_j} / \tau_C \tag{9}$$

4.3. Modeling of the Spatial and Time Characteristics of Flow Instabilities

The flow instabilities are here characterized based on their spatial characteristic wavelength and their characteristic time periodicity (or frequency) of the surface and volume distortions. Wavelength λ is defined as the average spatial distance between two consecutive similar distortions (**Figure 5**). The characteristic time periodicity is obtained by three methods. First, identified via offline optical analysis is undertaken on the already collected extrudates at room temperature. Offline optical characteristic time periodicity $\tau_{\text{Char.}}^{*,\text{offline}}$ is defined as the ratio of the wavelength λ and the extrudate velocity $V_{\text{ext.}}$ (Equation (10))

$$\tau_{\text{Char.}}^{*,\text{offline}} = \lambda / V_{\text{ext.}} \left(f_{\text{Char.}}^{\text{offline}} = V_{\text{ext.}} / \lambda\right) \tag{10}$$

In case of multiple wavelengths, for example, in case of stick-slip, more than one periodicities are obtained. In terms of stick-slip instability, one extrudate velocity is assumed, which is obtained by Equation (6), and the characterization takes place in both regions, stick and slip.

Second, online optical characteristic periodicity $\tau_{\text{Char.}}^{*,\text{online}}$ is defined as the time between two consecutive similar events in the space–time diagram (Figure 3c). The advantage of the online optical characteristic periodicity is that it does not use any estimated or assumed value like the extrudate velocity. Third, the Fourier transform (FT) analysis of the pressure signal from the piezoelectric transducers, $\tau_{\text{Char.}}^{*,\text{FT pressure}}$ can also be used to give the characteristic time periodicity.[8,9,11,23]

The spatial characteristic wavelength λ can be obtained by the proposed model, Equation (11), from Wang et al.[29] and Barone *et al.*[30] For round capillary dies (circular cross-section area), the spatial characteristic wavelength λ of flow instabilities is correlated with the diameter of the die D, the swelled diameter of the extrudate D', instability time periodicity τ^*, and the apparent shear rate $\dot{\gamma}_{\text{app.}}$. The value of the swelled diameter D', as defined within this study, is the average value from the collected extrudates as obtained by the capillary extrusion dies

$$\lambda^{\text{Capillary}} = \frac{D}{8}\left(\frac{D}{D'}\right)^2 \dot{\gamma}_{\text{app.}}\tau^* \tag{11}$$

Equation (11) results from the following condition, $\lambda = V\tau^*$. The average extrudate velocity is given by the product of extrudate velocity and the die swell factor, $V = V_{\text{extr.}}(D/D')^2$.[29] The extrudate velocity for round capillary and slit dies is given by

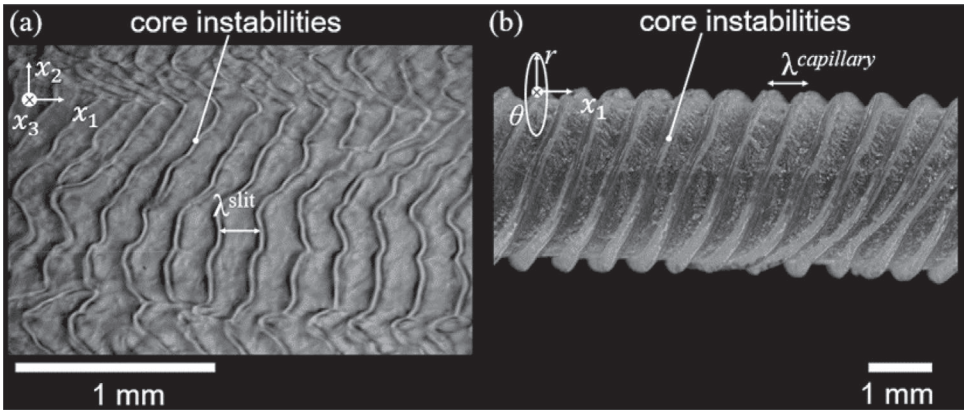

Figure 5. Offline optical analysis with a) transmission polarization microscopy for a rectangular shape extrudate at $\dot{\gamma}_{app.}^{Slit} = 20\ s^{-1}$ and b) incident light microscopy for a cylindrical shape extrudate at $\dot{\gamma}_{app.}^{Capillary} = 10\ s^{-1}$ for SBR A at 120 °C. The x_1 indicates the extrusion direction. At both images there is indication for the typical spatial characteristic wavelength. The core instability indication refers to the main flow instability which is observed in the extrudate.

$V_{extr.}^{Capillary} = (D/8)\dot{\gamma}_{app.}$ and $V_{extr.}^{Slit} = (H/6)\dot{\gamma}_{app.}$, respectivly. Equation (11) is modified for the slit die, including two contributions of swelling influence for W (x_2) and H (x_3) directions (Equation (12) and Figure 2). Then, W' and H' are the swelled width and heigth of the rectagular shape extrudate. For the detailed derivation of Equation (12), see Appendix A. Consistent with our experimental observations from the extrudates, it is assumed that $(H/H') \approx 1$. Thus, Equation (12) becomes (13)

$$\lambda^{Slit} = \frac{H}{6}\left(\frac{H}{H'}\frac{W}{W'}\right)\dot{\gamma}_{app.}\tau^* \tag{12}$$

$$\lambda^{Slit} = \frac{H}{6}\left(\frac{W}{W'}\right)\dot{\gamma}_{app.}\tau^* \tag{13}$$

Assuming the same range of shear rates for both geometries (slit and round capillary), the following relationship arises

$$\dot{\gamma}_{app.}^{Capillary} = \dot{\gamma}_{app.}^{Slit} \Rightarrow V^{Capillary}\left(\frac{D}{8}\right)^{-1}\left(\frac{D'}{D}\right)^{2} = V^{Slit}\left(\frac{H}{6}\right)^{-1}\left(\frac{H'}{H}\frac{W'}{W}\right) \tag{14}$$

where D is the diameter of the round capillary, and H is the height of the slit die. Consistent with our experimental observations from extrudates of the same material obtained by slit and round capillary dies, $(D'/D)^2 \approx [(W'H')/(HW)]$. Hence, $V_{extr.}^{Capillary} = (6D/8H)V_{extr.}^{Slit}$, where in this case $D = 2$ mm and $H = 0.5$ mm, so $V_{extr.}^{Capillary} = 3V_{extr.}^{Slit}$ for the same apparent shear rate.

The characteristic frequency $f_{Char.}$, for the flow instabilities of a specific PBD ($M_w = 182$ kg mol^{-1}, $Đ = 1.9$) sample at 50 °C, has been reported by Inn et al.,[41] and Barone et al.[42] that increased following a power law function of the shear stress to the ≈2nd power, $f_{Char.} \propto \sigma^2$. In the present study, the $f_{Char.}$ for the flow instabilities of the investigated SBR samples at 120 °C has been experimentally observed that behave as a power law function of the shear stress to the ≈2.5 power, $f_{Char.} \propto \sigma^{2.5}$. Knowing the power law dependency of the shear stress by the shear rate, $\sigma(\dot{\gamma}) = K\dot{\gamma}^n$ (Table 3), this study suggests that

$$f_{Char.} = \frac{1}{\tau^*} = a\dot{\gamma}_{app.}^{0.5} \tag{15}$$

where a is a constant and assumed to be material dependent.

5. Results and Discussion

5.1. 2D SEC-NMR Technique

A new combined method[36] using a low field benchtop NMR (62 MHz, 1.45 Tesla, ^{1}H) spectrometer coupled to SEC was used to correlate the molecular weight distribution and the chemical composition of the SBR samples. For the SBRs, the sequence distribution and chemical composition have the dominating influence on the mechanical and physical properties. The latter facilitates the fundamental understanding of structure–properties relationship.

The 2D SEC-NMR technique[36] is used to investigate the multimodality with respect to the correlation of molecular weight distribution and chemical composition. **Figure 6** illustrates the 2D SEC-NMR contour plots, including the respective normalized 1D NMR spectra and SEC elugram plots. As evident from Figure 6a,b, there are two distinct components, at an elution volume of ≈40 and ≈60 mL, with their resulting ^{1}H-NMR resonance groups. According to ^{1}H-NMR spectra, the first fraction at an elution volume of ≈40 mL in both Figure 6a,b, it is ascribed to SBR. Additionally, the second fraction at an elution volume of ≈60 mL is identified as low molecular weight hydrocarbon species. As the measurements were performed at nonquantitative NMR conditions, i.e., the free induction decay (FID) acquisition length of the analyte was $<5 \times T_1$, where T_1 is the longest longitudinal relaxation time, therefore only semi-qualitative comparisons can be made.[46] Comparing the ^{1}H-NMR spectra qualitatively between Figure 6a and b, the results indicate that sample A has a higher amount of 1,2 butadiene isomer relative to B ($\delta = 4$–6 ppm). This result is in agreement with the high field ^{1}H-NMR results (Table 2). An estimation on the amount of low molecular weight hydrocarbons relative

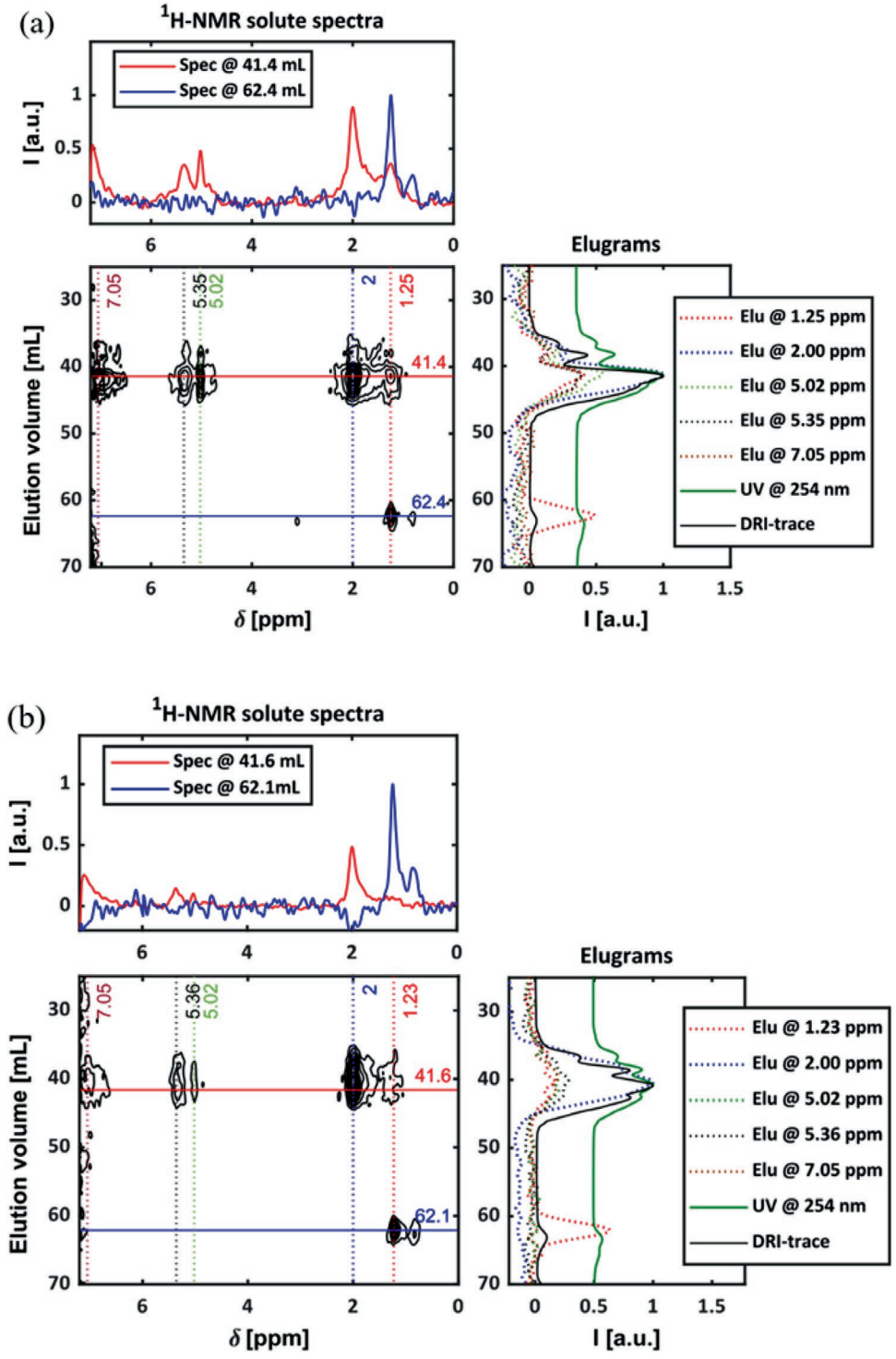

Figure 6. 2D SEC-NMR data for a) SBR A and b) SBR B in $CHCl_3$, with the corresponding 1D elugrams and 1D ^{1}H-NMR solute spectra. Data acquisition per spectrum, 90° pulse, 500 ms repetition time, 4 scans/spectrum. The SEC is equipped with a semi-preparative column with length of 300 mm and inner diameter of 20 mm, enabling the MWD and chemical composition correlation. Consequently, the elution volume differs from Figure 1 which has an analytical column with length of 300 mm and inner diameter of 8 mm.

to the SBR components within SBR A and B was conducted by performing a 2D integration. It is found, qualitatively, that sample A and B contains about 5% and 6% in weight fraction of the low molecular weight hydrocarbon component, respectively.

5.2. Linear and Nonlinear Rheology

The investigated samples have similar multimodal MWD with relatively similar weight composition of each mode. Specifically,

the MWD (Table 1) of both SBRs have a bimodal behavior. The high molecular weight tail ($M_w \approx 757$ kg mol^{-1} for the SBR A, and $M_w \approx 650$ kg mol^{-1} for the SBR B) and the medium molecular weight component ($M_w \approx 260$ kg mol^{-1} for the SBR A, and $M_w \approx 256$ kg mol^{-1} for the SBR B) have rather similar fractions for both of the polymer samples. The influence of the high molecular weight amount on the linear viscoelasticity needs to be discussed. The study of Wasserman and Graessley[45] has shown that differences of about ≈1.2% high molecular weight fraction between two linear polystyrene melts could increase G' almost four times in the terminal flow regime.[45]

The linear viscoelasticity of the two investigated materials has been obtained by oscillatory frequency sweep in a wide range of temperatures (–45 to +120 °C). **Figure 7**a presents the master curve of G' and G'' as a function of angular frequency (10^{-3} to 10^{10} rad s^{-1}) over 13 decades at reference temperature of 120 °C. None of the two samples have reached the terminal zone where both $G' \propto \omega^2$ and $G'' \propto \omega^1$. The longest relaxation time of the material τ_d is the reptation time and can be obtained by the inverse of the existing crossover from G' and G'' for polymers with narrow MWD and linear molecular architecture. For complex molecular architectures and broad or bimodal MWDs, different approaches for the determination of the reptation time have been suggested in literature, for example, the double reptation theory.[18] For simplicity within this study, the reptation time is determined by the inverse of the existing crossover from $G'$and G''. Although owing to the multimodality of the samples, the relaxation time is named as the overall relaxation

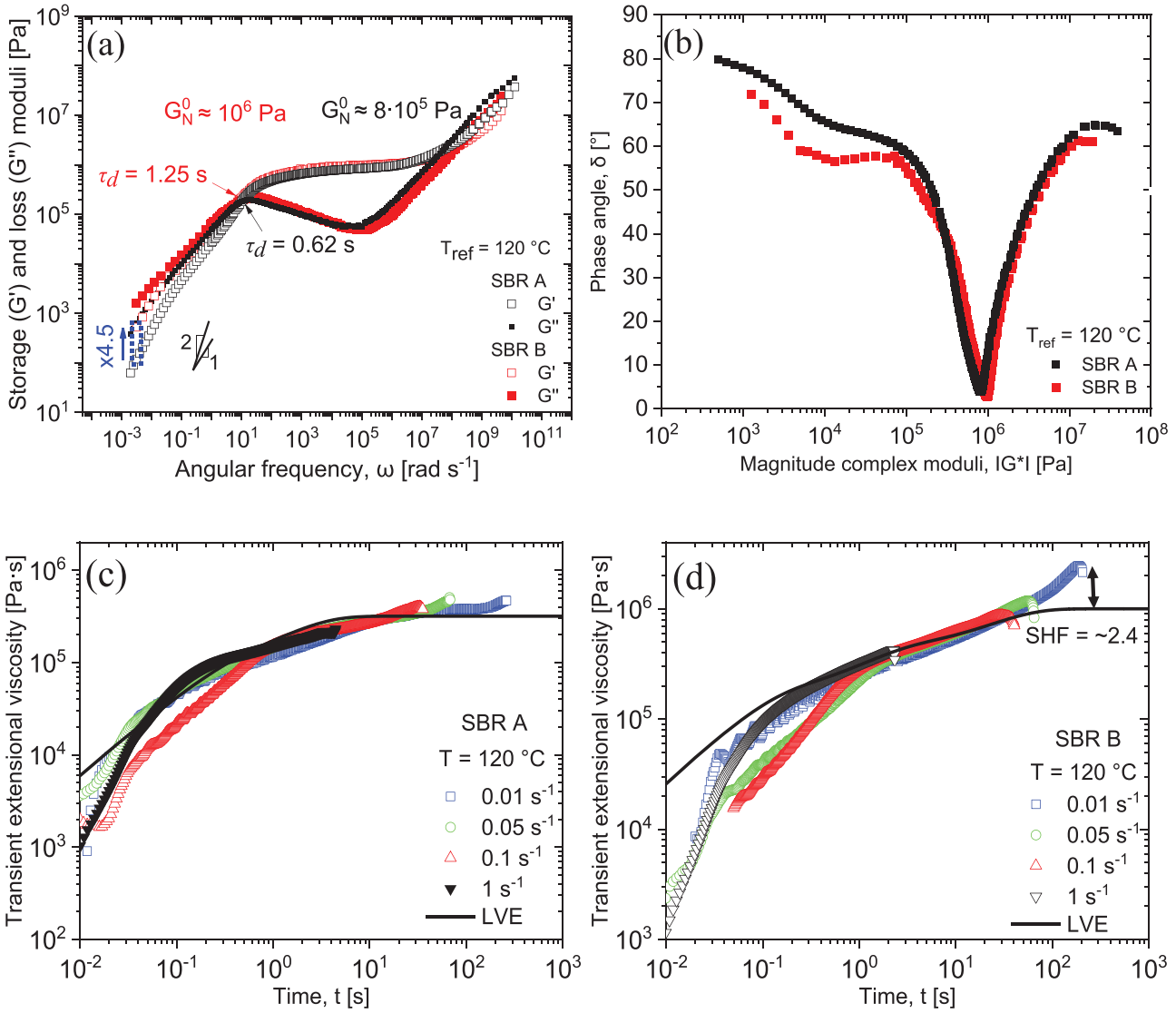

Figure 7. a) Comparison of the master curves of the two investigated samples at reference temperature of 120 °C. Storage and loss moduli as a function of angular frequency; the longest relaxation time of the SBR B is almost double than the SBR A. b) The van Gurp–Palmen plot indicates a different behavior between the two samples below $|G^*| < 3\ 10^5$ Pa. This difference can be associated with the existence of branches. c,d) Transient nonlinear extensional viscosity for both materials at 120 °C. d) SBR B presents strain hardening at $\dot{\varepsilon} = 0.01$ s^{-1} which indicates the existence of low degree branched molecules.

time, because it takes into account the contributions from all the molecular weight components. The SBR B has almost double the relaxation time τ_d than the SBR A, specifically $\tau_{d,\,SBR\,B} = 1.25$ s and $\tau_{d,\,SBR\,A} = 0.62$ s at 120 °C. It is known[6,47] that the relaxation time dependents on the number of entanglements to the third power, $\tau_{d,\,SBR\,B}/\tau_{d,\,SBR\,B} \approx (Z_{SBR\,B}/Z_{SBR\,A})^3$. Knowing[6,47] that $G_N^0 \approx \rho RT / M_e \approx Z\rho RT / M_w$ and the ratio of the plateau modulus values, $G^0_{N,SBR\,B} / G^0_{N,SBR\,A} \approx 1.25$ (Figure 7a). Then, the difference of the longest relaxation times between the samples is explained by the different number of entanglements, $\tau_{d,SBR\,B} / \tau_{d,SBR\,A} \approx (Z_{SBR\,B} / Z_{SBR\,A})^3 \approx (G^0_{N,SBR\,B} / G^0_{N,SBR\,A})^3 \approx 2$. Moreover, observing the G' over three decades, from 10^{-3} to 10^{1} rad s^{-1}, of angular frequency and specific at $\omega = 0.0032$ rad s^{-1} the value of G' for the SBR A is ≈4.5 times lower than the value of G' for the SBR B. This is explained by the difference in the high molecular weight tail of the MWD (Table 1). To investigate the molecular architecture of the samples, the van Gurp–Palmen plot is presented in Figure 7b. The plot exhibits a difference between the two samples at magnitude of complex moduli below $|G^*| < 3 \times 10^5$ Pa. Both samples at $|G^*| \approx 10^4$ Pa present a second relaxation process which can be associated with the existence of branches.[48,49] The phase angle of SBR B has lower values than SBR A at $|G^*| \approx 10^4$ Pa which implicates the existence of higher volume fraction and/or higher molecular weight branches. Usually, nonlinear transient extensional rheology is used to investigate the existence of branches via the strain hardening effect in polymer melts.[48,49] Figure 7c,d presents the transient extensional viscosity for both materials at four different extensional rates $\dot{\varepsilon}$. For the SBR A (Figure 7c), an indication for strain hardening is presented at $\dot{\varepsilon} = 0.01$ and 0.05 s^{-1}, however at $\dot{\varepsilon} = 0.1$ and 1 s^{-1} no existence of hardening is observed. For the SBR B (Figure 7d), at $\dot{\varepsilon} = 0.01$ s^{-1} strain hardening is detected with a strain hardening factor (SHF) of about ≈2.4. The other investigated extensional rates do no present strain hardening.

Based on the rheological characterization in the linear and nonlinear regime for both SBR samples, it can be stated that the SBR B has more and/or longer branches than the SBR A. This is confirmed by the van Gurp–Palmen plot (Figure 7b) and the extensional nonlinear rheology (Figure 7d). According to Stadler et al.,[53,54] such a strain hardening behavior at low extensional rates $\dot{\varepsilon}$ is usually observed for samples with a fairly low degree of branching which belong to the high molecular weight tail.

To investigate the processing flow behavior in a controlled way, capillary rheology experiments were carried out with round capillary and slit dies. The raw round capillary die data were further processed by Bagley[4] and Rabinowitsch-Weissenberg[4] corrections using a series of three round capillary dies with length-to-diameter ratios of $L/D = 5$, 10, 15 and $D = 2$ mm at 120 °C. The viscosity data from the round capillary die with $L/D = 15$ are presented in Figure 8. For the slit die with $L/H = 60$, only Rabinowitsch-Weissenberg[4] correction is applied. The $L/H = 60$ allows to neglect exit pressure influence, thus the wall shear stress is directly obtained from pressure values.[4] The empirical relationship Cox-Merz rule[50] has been applied to our data (**Figure 8**). The Cox-Merz rule implies a universal relation between linear oscillatory shear and the nonlinear steady-state shear. This rule states that the shear rate dependency of

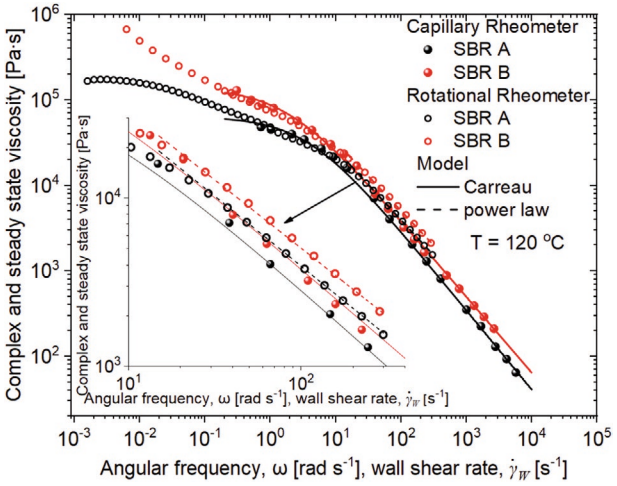

Figure 8. Magnitude of complex viscosity as a function of angular frequency obtained by oscillatory shear frequency sweep experiments and the steady-state shear viscosity as a function of wall shear rate obtained by capillary experiment. The capillary data are Bagley[4] and Rabinowitsch-Weissenberg[4] corrected for the $L/D = 15$ with $D = 2$ mm round capillary die.

the steady-state viscosity $\eta(\dot{\gamma})$ is equal to the magnitude of the complex viscosity $|\eta^*(\omega)|$, that is, $\eta(\dot{\gamma}) = |\eta^*(\omega)|$, with the numerical values of $\dot{\gamma} = \omega$.[50] The viscosity data of the SBR A and B are presented in Figure 8. Despite the bimodal MWD and the existence of branching molecular architecture Cox-Merz rule appears to be valid for shear rates below $\dot{\gamma}_w < 20$ s^{-1}. Deviation between the capillary and rotational rheometer data is detected for shear rates/angular frequencies higher than $\dot{\gamma}_w > 20$ s^{-1} (Figure 8). Then, the shear viscosity data from capillary rheology are below the magnitude of the complex viscosity data from oscillatory rheology. The deviation of the Cox-Merz rule for both samples starts at similar shear rate, $\dot{\gamma}_w \approx 20$ s^{-1}. This is explained by the bimodal MWD, molecular architecture, and the similar amount of low MW component. According to Inn,[14] the Cox-Merz rule fails at high shear rates/angular frequencies for bimodal MWD as the amount of low MW component increases at the wall. This observation is explained based on the segregation theory.[51] During fast flow ($\dot{\gamma} > 1/\tau_d$) longer chains acquire more elastic energy near the wall than shorter ones, which creates forces that lead to segregation of longer chains away from the wall toward the centerline (low shear stress area). Similarly, shorter chains would potentially migrate toward the wall (high shear stress area).[51] Hence, the slippage becomes stronger as the amount of low MW components increased at the wall.[14]

The Carreau model,[38] Equation (1), was used to fit the capillary data and quantify the difference between them. At high shear rates/angular frequencies after $\dot{\gamma}_w > 20$ s^{-1}, where the shear-thinning behavior happens, it is observed for both viscosities a difference of a factor ≈1.3. At those high shear rates, the flow is not influenced by MWD. In contrast, between $\dot{\gamma}_w = 0.03$ and 20 s^{-1}, where the MWD has the dominant influence on the flow, the two materials exhibit difference by a factor of ≈2.

In addition, the power law model, Equation (2), was used to fit the shear rate dependent (shear-thinning) viscosity data

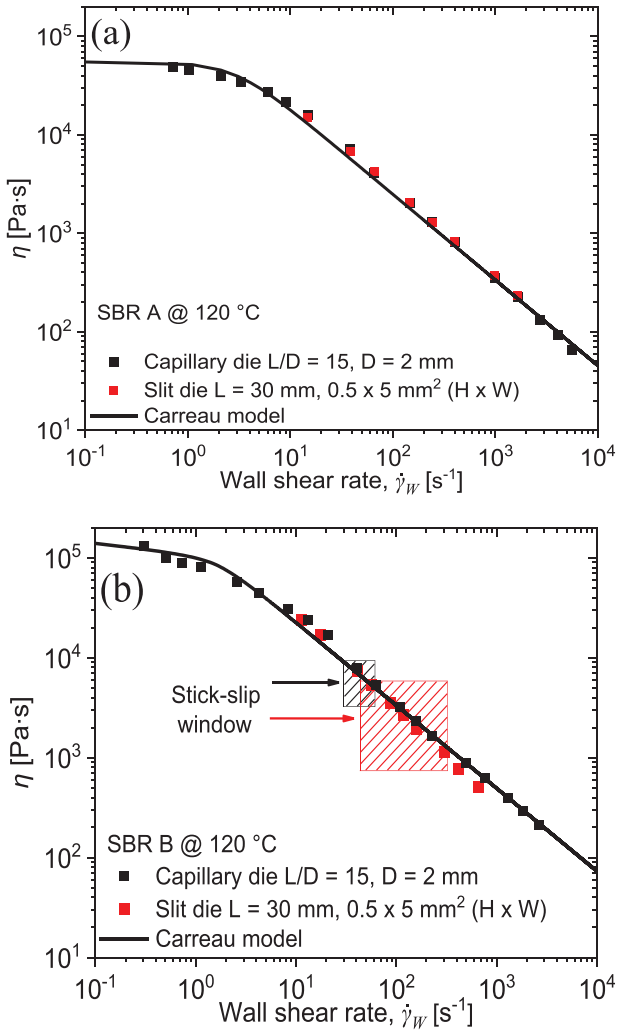

Figure 9. a) Absolute values of the steady-state viscosity as a function of wall shear rate $\dot{\gamma}_w$ for slit and round capillary dies. Agreement between both geometries is observed for (a) SBR A where only sharkskin instability appears. Deviation between the two geometries occurs for (b) SBR B after $\dot{\gamma}_w > 30$ s^{-1} where the stick-slip instability appears at the slit die between $\dot{\gamma}_w \approx 40$ and 300 s^{-1}; afterward, gross melt fracture instability occurs. b) The shear rate range of the stick-slip instability for the SBR B material at the round capillary and slit dies is displayed by the shaded areas in the plot.

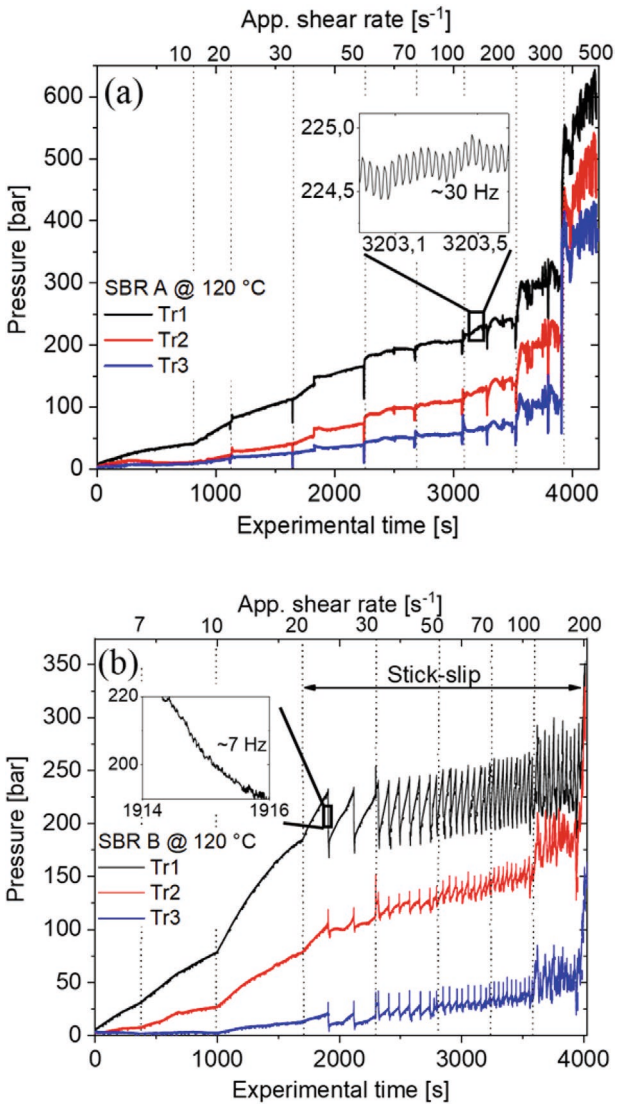

Figure 10. Profile of pressure signal during capillary extrusion at 120 °C, as detected by the three piezoelectric transducers within the slit die. The dimensions of the slit die are $L = 30$ mm and 0.5×5 mm^2 ($H \times W$) cross-section area. a) SBR A presenting sharkskin and an enlarged part of the pressure profile from Tr1 to depict the pressure oscillations. b) SBR B presenting sharkskin up to $\dot{\gamma}_{app} = 20$ s^{-1} and afterward stick-slip up to $\dot{\gamma}_{app} = 200$ s^{-1}.

from rotational rheometry at the region where the Cox-Merz rule fails. Thus, material parameters K (consistency index) and n (flow index) were obtained and used for the computation of the slip velocity. The fitting values of the models are listed in Table 3.

Steady-state viscosity curves from slit and round capillary dies are presented in **Figure 9**. The absolute values of steady-state viscosity are similar between the two geometries for the SBR A (Figure 9a). Although, in Figure 9b, deviation of the steady-state viscosity between the two geometries is detected after $\dot{\gamma}_w \approx 30$ s^{-1} owing to the onset of stick-slip instability in the slit die for the SBR B sample. During the extrusion of SBR B with two different dies, it was found that this material in the round capillary die presents stick-slip instability within the shear rate range $\dot{\gamma}_w \approx 30$–60 s^{-1}. However, in the slit die the stick-slip instability is observed at $\dot{\gamma}_w \approx 40$–300 s^{-1} for SBR B sample. Hence, according to experimental observations the stick-slip instability occurs over a wider range of shear rates in the slit die than the round capillary die for the SBR B sample. For this reason, the viscosity data from the slit die have a slight deviation from the round capillary die (Figure 9b).

Figure 10 presents the raw pressure signal from the three piezoelectric pressure transducers of the slit die for the SBR A and B at similar shear rates. Figure 10a depicts the behavior of the pressure signal during sharkskin within $\dot{\gamma}_{app.} = 10$ and 200 s^{-1}, and Figure 10b during sharkskin and stick-slip flow instabilities within $\dot{\gamma}_{app.} = 7$ and 20 s^{-1}, and $\dot{\gamma}_{app.} = 30$ and

200 s^{-1}, respectively. Selected optical visualizations of the extrudates are given by **Figures 11**a and **12a**. Data are recorded for about 500 s, at each shear rate to capture both types of flow instabilities. In Figure 10a, sharp peaks are observed any time that the shear rate is changed owing to the collection of the extrudates. Because of the inherent detection mechanism of the piezoelectric transducers, absolute values of the pressure signal are not reliable.[52] Nevertheless, the pressure fluctuations at a given shear rate provide the characteristic frequency of the flow instability via the already discussed data analysis.[8,9,23–25]

5.3. Offline and Online Optical Analysis

Using the offline optical analysis techniques, the collected extrudates were investigated at room temperature. In Figure 11a, selected extrudates obtained by the slit die for the SBR A at 120 °C are presented. The extrudates have been investigated by transmission polarization microscopy at $\dot{\gamma}_{app}$ = 30, 50, 70, 100, 200, and 500 s^{-1}. Figure 11b presents selected extrudates obtained by the round capillary die for the SBR A as they investigated by incident light microscopy at $\dot{\gamma}_{app}$ = 7, 10, 30, 70, 100, and 500 s^{-1}. For the SBR A sample, a stick-slip instability is not presented.

In Figure 12a, selected extrudates with stick-slip instability obtained by the slit die for the SBR B at 120 °C are presented. As mentioned before the stick-slip instability is separated into two regions, stick and slip parts. Both regions at apparent shear rates of $\dot{\gamma}_{app}$ = 30, 50, and 70 s^{-1} are presented. Figure 12b presents selected extrudates obtained by the round capillary die for the SBR B as they investigated by incident light microscopy

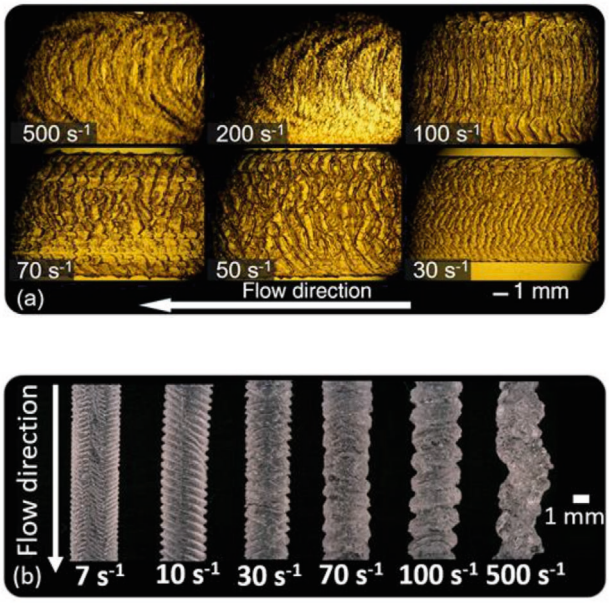

Figure 11. Offline optical analysis of SBR A extruded at 120 °C by a) transmission polarization microscopy and b) incident light microscopy. Extrudates from a) slit die of H = 0.5 mm, W = 5 mm, and L = 30 mm and b) round capillary die of L/D = 15 with D = 2 mm. The apparent shear rate $\dot{\gamma}_{app}$ is mentioned at each extrudate.

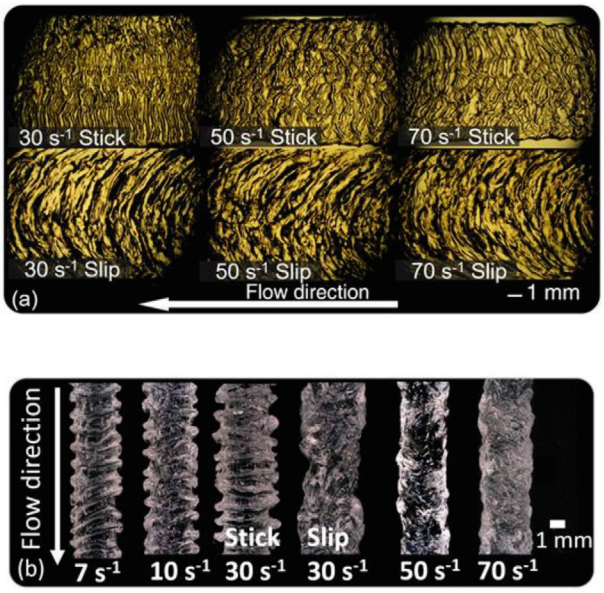

Figure 12. Offline optical analysis of SBR B extruded at 120 °C by a) transmission polarization microscopy and b) incident light microscopy. Extrudates with the stick-slip instability from a) slit die of H = 0.5 mm, W = 5 mm, and L = 30 mm in the shear rate range between $\dot{\gamma}_{app}$ = 30 and 70 s^{-1} and b) round capillary die of L/D = 15 with D = 2 mm at $\dot{\gamma}_{app}$ = 30 s^{-1}. The apparent shear rate $\dot{\gamma}_{app}$ is mentioned at each extrudate.

at $\dot{\gamma}_{app}$ = 7, 10, 30, 50, and 70 s^{-1}. Stick-slip instability for the obtained by the round capillary die extrudates has been observed at $\dot{\gamma}_{app}$ = 30 s^{-1}, both regions, stick and slip, are presented separately.

Observing the extrudates obtained by the slit die at Figures 11a and 12a the proposed definitions[8,9,11] of sharkskin and stick-slip met flow instabilities agree with the appearance of the extrudates. However, noticing the extrudates obtained by the round capillary die at Figures 11b and 12b, only the extrudate $\dot{\gamma}_{app}$ = 7 s^{-1} for the SBR A can be categorized as surface instability and possibly designated as sharkskin. The rest of the extrudates obtained by the round capillary die can be categorized as volume instability and generally named as melt fracture or spurt.[5,10] For both Figures 11b and 12b, the spatial characteristic wavelength of the flow instability can be identified. Based on the spatial characteristic wavelength of the flow instability, the extrudate distortions can be quantified, regardless of the type of flow instability.

Using the online optical analysis technique during the extrusion of the samples by the slit die, space–time diagrams have been constructed for each shear rate, and the characteristic time periodicity of the flow instabilities is investigated. In **Figure 13**, space–time diagrams for SBR A at $\dot{\gamma}_{app}$ = 10 and 30 s^{-1} are presenting sharkskin instability at 120 °C. In **Figure 14**, selected space–time diagrams for $\dot{\gamma}_{app}$ = 10 and 70 s^{-1} of the SBR B are presented at 120 °C. In Figure 14a, the sharkskin flow instability is presented at $\dot{\gamma}_{app}$ = 10 s^{-1}, while in Figure 13b the stick-slip instability is captured at $\dot{\gamma}_{app}$ = 70 s^{-1}. For both Figures 13 and 14 at each space–time diagram, a snapshot for a specific region of the extrudate is shown enlarged, and the characteristic time periodicity can be better visualized.

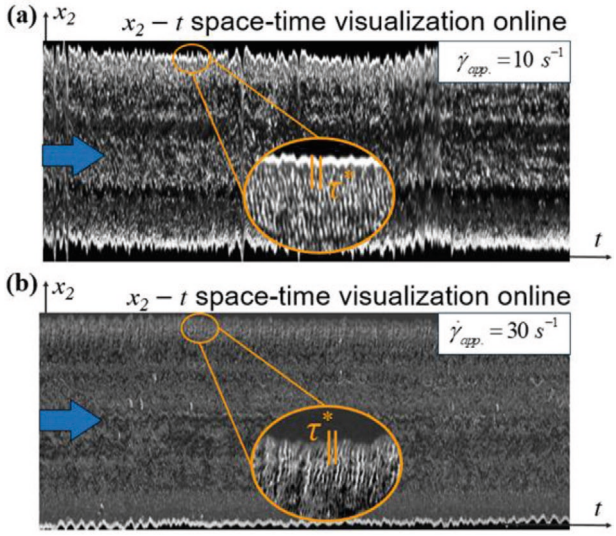

Figure 13. Space–time diagram of the SBR A at 120 °C for two different apparent shear rates $\dot{\gamma}_{app}$ obtained by the slit die. The extrudate a) at $\dot{\gamma}_{app}$ = 10 s^{-1} and b) at $\dot{\gamma}_{app}$ = 30 s^{-1} exhibit sharkskin instability. At each diagram a snapshot for a specific region of the extrudate is displayed enlarged, and the characteristic periodicity can be identified. The blue arrows indicate the extrusion direction.

5.4. Slip, Extrudate, and Average Stick-Slip Velocities

Using Equations (4) and (5) slip velocities[3] are obtained for both geometries (**Figure 15**a). The slip velocity of each material as a function of wall shear stress presents a master curve independent of the die geometry. The investigated samples seem

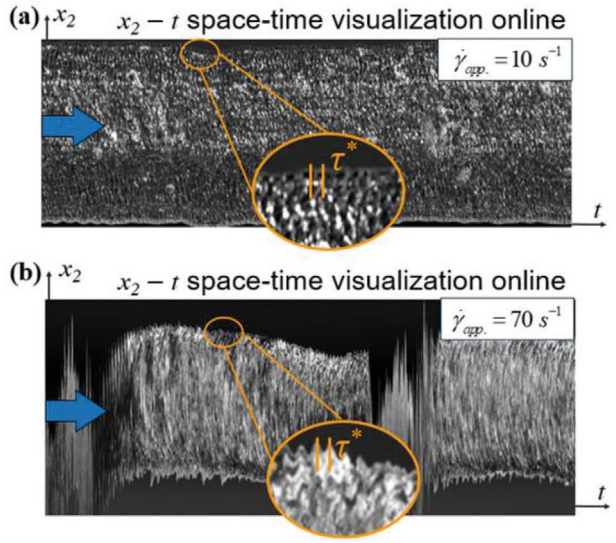

Figure 14. Space–time diagram of the SBR B at 120 °C for two different shear rates obtained by the slit die. The extrudate a) at $\dot{\gamma}_{app}$ = 10 s^{-1} exhibits sharkskin instability and b) at $\dot{\gamma}_{app}$ = 70 s^{-1} two stick-slip oscillations are presented. At each diagram a snapshot for a specific region of the extrudate is displayed enlarged, and the characteristic periodicity is identified. The blue arrows indicate the extrusion direction.

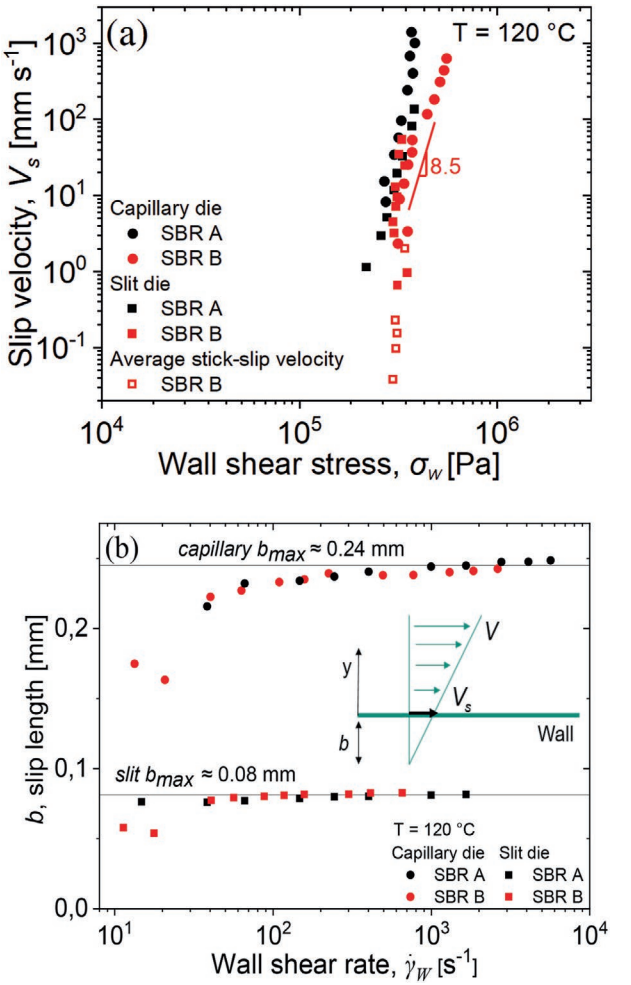

Figure 15. a) Slip velocity, average stick-slip velocity, and b) slip length calculated from Equations (4), (5), (9), and (7), respectively. Using the interfacial rheological law,[37] it is found that $b^{Capillary} \approx 3b^{Slit}$, where b_{max} is the maximum slip length. The round capillary die has dimensions of L/D = 15 with D = 2 mm and the slit die dimensions of H = 0.5 mm, W = 5 mm, and L = 30 mm.

to behave slightly different with SBR A to present higher slip velocities at $\sigma_W > 5\ 10^5$ Pa than the SBR B.

Applying the interfacial rheological law,[39] Equation (7), the slip length for both geometries is obtained (Figure 15b). As expected, the slip length in the slit die is approximately three times lower than in the round capillary die. In addition, both materials have similar slip length despite displaying different types of flow instabilities.

The computed values by Equation (9) for the average stick-slip velocity $V_{stick\text{-}slip}$ for the SBR B material are presented as well (Figure 15a). The cross-correlation time which is obtained by the first maximum of Equation (8) represents the time that a whole pressure oscillation, that is, a stick-slip event, travels from Tr_i to Tr_j (**Figure 16**). The duration of the stick-slip is quite large because both contributions are taken into account, that is, the stick part which is the pressure buildup and the slip part which is the rapid pressure drop (Figure 4b).

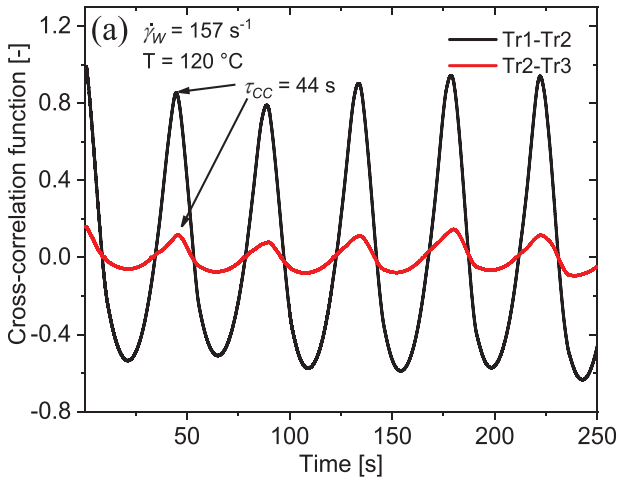

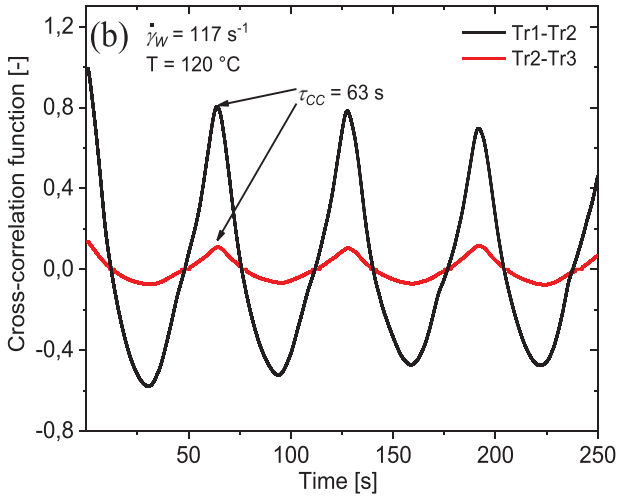

Figure 16. Cross-correlation function, see Equation (8), of the Tr1–Tr2 and Tr2–Tr3 for the SBR B at 120 °C during stick-slip instability at two different shear rates.

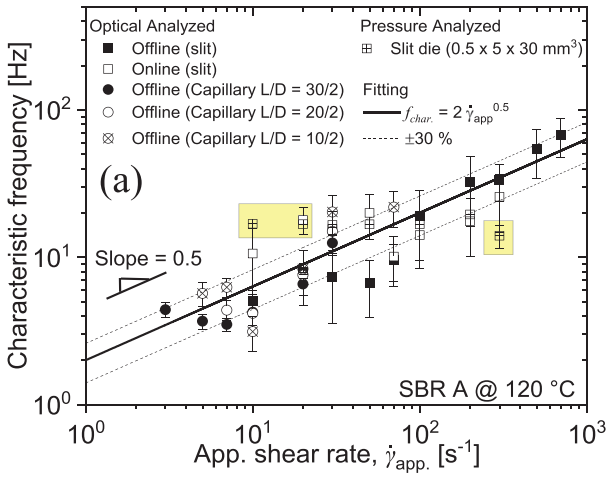

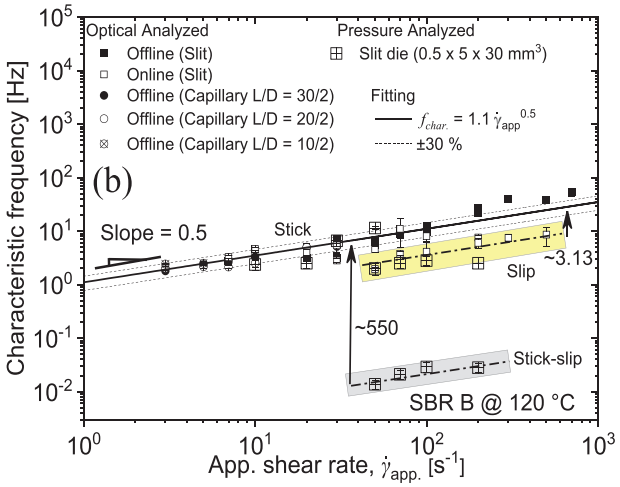

Figure 17. a,b) Characteristic frequency of the flow instability as measured by the three different techniques, online, offline optical analysis, and highly pressure sensitive slit die for SBR A and SBR B, respectively. In (a) the highlighted regions represent the deviation of more than 30% from the fitting, and in (b) the yellowish highlighted region depicts the low-frequency components which are caused by the slip part of the extrudate, and the grayish highlighted region depicts the characteristic frequency of the stick-slip pressure oscillation.

5.5. Time and Spatial Characteristics of Flow Instabilities

The characteristic frequency (or periodicity) of the flow instability was obtained and compared for both slit and round capillary dies. Especially, the highly pressure-sensitive slit die and the online optical analysis for the slit die were used for both materials. The collected extrudates from the slit and from all round capillary dies (L/D = 5, 10, 15 with D = 2 mm) were investigated by offline optical analysis at room temperature. In **Figure 17**a, the characteristic frequency of the SBR A is presented. All the optical analysis techniques, either online or offline, for the slit and for all the round capillary dies exhibit a linear increase behavior as a function of shear rate within $\dot{\gamma}_{app}$ = 3–700 s^{-1}. Regarding the highly pressure-sensitive slit die, a "plateau"-like trend is observed within $\dot{\gamma}_{app}$ = 10–300 s^{-1}. Observing the overall trend of the characteristic frequency, a monotonic linear increased as a function of shear rate in log-log scale can be asserted. Thus, the data are fitted by Equation (15), specifically for the SBR A, $f_{Char.} = 2\dot{\gamma}_{app.}^{0.5}$. The overall deviation of each technique from the fitting function is estimated to vary at most by 30%. Higher than 30% deviation from the fitting function is observed at low, $\dot{\gamma}_{app}$ = 10 and 20 s^{-1}, and one at high, $\dot{\gamma}_{app}$ = 300 s^{-1}, shear rates where the respective frequencies are obtained by the highly pressure-sensitive die. The respective frequencies are marked in Figure 17a.

In Figure 17b, the characteristic frequency as a function of apparent shear rate for the SBR B is presented. All the optical analysis techniques, either online or offline, for the slit and for all the round capillary dies exhibit a linear increase tendency as a function of shear rate within $\dot{\gamma}_{app}$ = 3–700 s^{-1} described by a power law behavior. Concerning the highly pressure-sensitive slit die, an increased trend is observed as well. Low-frequency components, below $f_{Char.} \approx 5$ Hz, are observed during the stick-slip instability above the $\dot{\gamma}_{app} > 30$ s^{-1} owing to side slide instabilities at the slip part of the extrudate (Figure 4a). Substantial

low-frequency components, $f_{Char.} \approx 10^{-2}$ Hz, are observed during the stick-slip instability above the $\dot{\gamma}_{app} > 30$ s^{-1} as well. These characteristic frequencies occur from the stick-slip pressure oscillation (Figure 4b).

Analyzing the characteristic frequency, a monotonic linear increase as a function of shear rate was fitted by a power law function such as $f_{Char.} = 1.1\dot{\gamma}_{app.}^{0.5}$. Similar to SBR A, the deviation of each technique from the fitting function is estimated to vary at most by 30% up to $\dot{\gamma}_{app} = 100$ s^{-1}. The low-frequency components within $\dot{\gamma}_{app} = 50$–500 s^{-1}, scale also with the power of 0.5 and differ by a factor of about ≈3.13 from the main fitting function (Figure 17b). This difference occurs owing to inherent variation in extrudate velocity within the stick-slip instability. In addition, above the $\dot{\gamma}_{app} > 200$ s^{-1} deviation from the fitting function is presented by the offline optical analyzed data as well. This deviation occurs owing to the difficulties to measure precisely the spatial characteristic wavelength of the distortions in the slip part of the extrudate (Figure 4a).

Knowing the fitting function for the characteristic frequency (or periodicity), the dimension of the die (D for round capillary, H and W for slit) and the swelled diameter D', Equations (11) and (13), can be used to predict the characteristic wavelength of the flow instabilities for round capillary and slit dies. Following the ratio between the extrudates velocities of $V_{extr.}^{Capillary} = 3V_{extr.}^{Slit}$, a similar behavior is expected to be found for the spatial characteristic wavelength as well. Assuming that the characteristic time periodity is material dependent and the swelling factor remains similar between the slit and round capillary geometries, the ratio of the spatial wavelength between the two geometries is given by $\lambda^{Capillary} = 3\lambda^{Slit}$ (**Figure 18**).

From quantitative point of view, for all the investigated round capillary dies (L/D = 5, 10, 15 with D = 2 mm) the spatial characteristic wavelengths of the instabilities do not deviate much of each other. Especially, observing Figure 18b, it appears that they have similar wavelegnth in the whole range of the investigated shear rates.

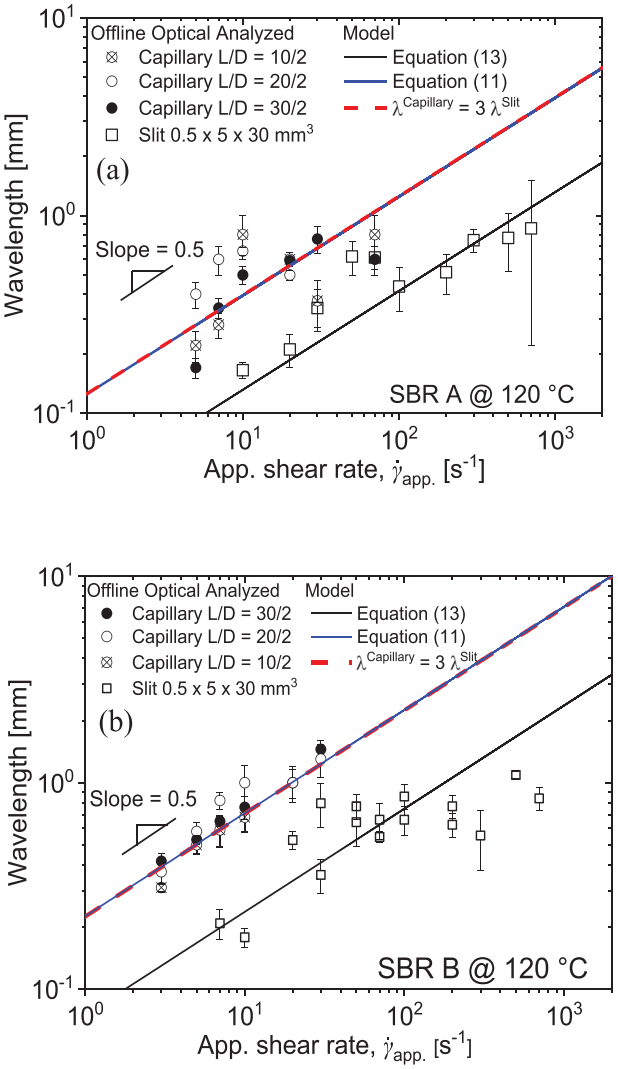

Figure 18. a,b) Characteristic spatial wavelength of the flow instability for SBR A and SBR B. The relationship for the spatial wavelength between the two geometries is described by $\lambda^{Capillary} = 3\lambda^{Slit}$. In (b) systematic deviation from the fitting function is observed at shear rates above $\dot{\gamma}_{app} > 100$ s^{-1}, this happens owing to difficulties to measure the wavelength of the distortions in the slip part of the slit-shaped extrudate.

6. Conclusions

Based on the obtained results, the following correlations between the molecular properties, rheological characterization, and extrusion flow are apparent for the investigated SBR samples:

1. SBR B has more or/and higher molecular weight branches than the SBR A. Both samples have about 5% (SBR A) and 6% (SBR B) of low molecular weight hydrocarbons. These two findings explain the differences in the zero shear viscosity and the different flow instabilities.
2. SBR polymers with similar MWD and chemical composition, but different isomer content of the butadiene monomer at the same temperature difference from the T_g disclose different types of flow instabilities during extrusion. At temperatures $T > T_g$ +100 °C the influence of the butadiene isomers is neglectable compared to the influence of the topological constraints (entanglements) and molecular architecture (linear, branched).
3. For the slit die (rectangular cross-section area) geometry, the stick-slip instability manifests itself in a broader range of shear rates compared to the round capillary (circular cross-section area) die for the investigated SBR B at 120 °C.
4. The characteristic frequency of the flow instabilities obtained by the highly sensitive slit die, offline and online optical analysis techniques can be fitted by a power law model as a function of shear rate to the power of 0.5, $f_{Char.} = a\dot{\gamma}_{app.}^{0.5}$.. The overall deviation of each technique from the fitting function is estimated to vary at most by 30%.
5. The qualitative model for the spatial characteristic wavelength, proposed by Wang et al.[29] and Barone et al.[30] for round capillary die, Equation (11), and its modification for slit die, Equation (13), are in agreement with the experimental data obtained from the SBR polymers for both die geometries.

6. Assuming the same range of shear rates for both slit and round capillary dies and given the dimensions of them, the modified version (Equation (13)) of the model proposed by Wang et al.[29] and Barone et al.[30] predicts the spatial characteristic wavelength from a round capillary to slit die and vice versa.

Appendix A

Volumetric flow rate Q inside the die is given by Equation (A1) and directly after the die exit by Equation (A2)

$$Q = W \cdot H \cdot V_{\text{extr.}}^{\text{Slit}} \tag{A1}$$

$$Q = W' \cdot H' \cdot \langle V \rangle \tag{A2}$$

Assuming no volume change, Equations (A1) and (A2) can be equated

$$\langle V \rangle = \left(\frac{W}{W'} \frac{H}{H'} \right) V_{\text{extr.}}^{\text{Slit}} \tag{A3}$$

knowing the extrudate velocity for slit die

$$V_{\text{extr.}}^{\text{Slit}} = (H/6)\dot{\gamma}_{\text{app.}} \tag{A4}$$

and then coupling Equations (A3) and (A4), Equation (A5) is derived

$$\langle V \rangle = \left(\frac{W}{W'} \frac{H}{H'} \right) (H/6)\dot{\gamma}_{\text{app.}} \tag{A5}$$

Defined[29,30] the spatial characteristic wavelength as

$$\lambda = \langle V \rangle \tau^* \tag{A6}$$

the analytical formula for the spatial characteristic wavelength for the slit die geometry is given by Equation (A7)

$$\lambda^{\text{Slit}} = \left(\frac{W}{W'} \frac{H}{H'} \right) (H/6)\dot{\gamma}_{\text{app.}} \tau^* \tag{A7}$$

Acknowledgements

The authors thank Pirelli Tyre S. p. A. for financial and sample support and for the permission to publish this work. Additionally, the authors would like to thank the fruitful discussions and support from Dr. Marianna Zinna, Mr. Luciano Garro, and the AiF-iGF 19925N project. Moreover, Mr. Lorenz Faust is acknowledged for his support to obtain and interpret the NMR spectra, Dr. Christopher Klein for the kind introduction to the optical microscopes, and Dr. Michael Pollard for proofreading the paper. The authors appreciate the useful comments from the anonymous reviewers.

Open access funding enabled and organized by Projekt DEAL.

Conflict of Interest

The authors declare no conflict of interest.

Data Availability Statement

Data available on request from the authors

Keywords

die geometry, flow instabilities, qualitative modeling, SBR, sharkskin

Received: December 22, 2020
Revised: February 4, 2021
Published online:

[1] A. Leonov, A. Prokunin, *Nonlinear Phenomena in Flows of Viscoelastic Polymer Fluids*, Chapman and Hall, London **1994**.
[2] M. M. Denn, *Ann. Rev. Fluid Mech.* **2001**, *33*, 265.
[3] S. G. Hatzikiriakos, *Prog. Polym. Sci.* **2012**, *37*, 624.
[4] S. G. Hatzikiriakos, K. Migler, *Polymer Processing Instabilities: Control and Understanding*, Marcel Dekker, New York **2005**.
[5] R. Koopmans, C. F. J. den Doelder, J. Molenaar, *Polymer Melt Fracture*, CRC Press, Boca Raton, FL **2011**.
[6] S. Q. Wang, *Nonlinear Polymer Rheology: Macroscopic Phenomenology and Molecular Foundation*, Wiley, New York **2017**.
[7] S. Q. Wang, in *Polymers in Confined Environments*, Vol. *1* (Eds: S. Granick, K. Binder, P. G. deGennes, E. P. Giannelis, G. S. Grest, H. Hervet, R. Krishnamoorti, L. Léger, E. Manias, E. Raphaël, S. Q. Wang), Springer-Verlag, Berlin **1999**, Ch. 6.
[8] I. F. C. Naue, Ph.D. Thesis, Karlsruhe Institute of Technology (KIT), Karlsruhe, Germany **2013**.
[9] I. F. .C. Naue, R. Kádár, M. Wilhelm, *Macromol. Mater. Eng.* **2015**, *300*, 1141.
[10] C. F. J. den Doelder, Ph.D. Thesis, Eindhoven University of Technology, Eindhoven, Netherlands **1999**.
[11] A. Gansen, M. Řehoř, C. Sill, P. Polińska, S. Westermann, J. Dheur, J. S. Hale, J. Baller, *J. Appl. Polym. Sci.* **2020**, *137*, 48806.
[12] H. Palza, S. Filipe, I. F. C. Naue, M. Wilhelm, *Polymer* **2010**, *51*, 522.
[13] M. Ansari, S. G. Hatzikiriakos, A. M. Sukhadia, D. C. Rohlfing, *Rheol. Acta* **2011**, *50*, 17.
[14] Y. W. Inn, *J. Rheol.* **2013**, *57*, 393.
[15] S. G. Hatzikiriakos, J. M. Dealy, *J. Rheol.* **1992**, *36*, 703.
[16] S. G. Hatzikiriakos, J. M. Dealy, *J. Rheol.* **1992**, *36*, 845.
[17] S. G. Hatzikiriakos, J. M. Dealy, *Int. Polym. Process.* **1993**, *8*, 36.
[18] M. Ebrahimi, T. Tomkovic, G. Liu, A. Doufas, S. G. Hatzikiriakos, *Phys. Fluids* **2018**, *30*, 053103.
[19] M. Ansari, S. G. Hatzikiriakos, A. M. Sukhadia, D. C. Rohlfing, *Polym. Eng. Sci.* **2012**, *52*, 795.
[20] O. Delgadillo-Velázquez, G. Georgiou, M. Sentmanat, S. G. Hatzikiriakos, *Polym. Eng. Sci.* **2008**, *48*, 405.
[21] M. Mooney, *J. Rheol.* **1931**, *2*, 210.
[22] S. Filipe, A. Becker, V. C. Barroso, M. Wilhelm, *Appl. Rheol.* **2009**, *19*, 23345.
[23] H. Palza, I. F. C. Naue, M. Wilhelm, *Macromol. Rapid Commun.* **2009**, *30*, 1799.
[24] H. Palza, I. F. C. Naue, S. Filipe, A. Becker, J. Sunder, A. Göttfert, M. Wilhelm, *Kautsch. Gummi, Kunst.* **2010**, *63*, 456.
[25] H. Palza, B. Reznik, M. Kappes, F. Hennrich, I. F. C. Naue, M. Wilhelm, *Polymer* **2010**, *51*, 3753.
[26] R. Kádár, I. F. C. Naue, M. Wilhelm, *Annu. Trans. - Nordic Rheol. Soc.* **2014**, *22*, 153.
[27] R. Kádár, I. F. C. Naue, M. Wilhelm, *Polymer* **2016**, *104*, 193.
[28] C. K. Georgantopoulos, I. F. C. Naue, A. Causa, L. Garro, M. Wilhelm, *Annu. Trans. - Nordic Rheol. Soc.* **2019**, *27*, 151.
[29] S. Q. Wang, P. A. Drda, Y. W. Inn, *J. Rheol.* **1996**, *40*, 875.

[30] J. R. Barone, N. Plucktaveesak, S. Q. Wang, *J. Rheol.* **1998**, *42*, 813.
[31] Y. W. Inn, R. J. Fisher, M. T. Shaw, *Rheol. Acta* **1998**, *37*, 573.
[32] F. N. Cogswell, *J. Non-Newtonian Fluid Mech.* **1977**, *2*, 17.
[33] A. Provenzale, L. Smith, R. Vio, G. Murante, *Physica D* **1992**, *58*, 31.
[34] C. S. Dutcher, S. J. Muller, *J. Fluid Mech.* **2009**, *641*, 85.
[35] R. Kádár, C. Balan, *Eur. J. Mech. B* **2012**, *31*, 158.
[36] C. Botha, J. Höpfner, B. Mayerhöfer, M. Wilhelm, *Polym. Chem.* **2019**, *10*, 2230.
[37] D. van Dusschoten, M. Wilhem, *Rheol. Acta* **2001**, *40*, 395.
[38] F. A. Morrison, *Understanding Rheology*, Oxford University Press, Oxford **2001**.
[39] F. Brochard-Wyart, P. G. Gennes, *Langmuir* **1992**, *8*, 3033.
[40] J. Honerkamp, *Stochastic Dynamic Systems: Concepts, Numerical Methods, Data Analysis*, Wiley-VCH, New York **1994**.
[41] Y. W. Inn, L. Wang, M. T. Shaw, *Macromol. Symp.* **2000**, *158*, 65.
[42] J. R. Barone, S. Q. Wang, Paper IR6, SoR 70th Annual Meeting, **1998**.
[43] M. Maurice, *Rubber Technology*, Springer Science + Business Media, Dordrecht, The Netherlands **1999**.
[44] H. E. Railsback, N. A. Stumpe, *Rubber Age* **1975**, *27*, 101.
[45] S. H. Wasserman, W. W. Graessley, *J. Rheol.* **1992**, *36*, 543.
[46] R. R. Ernst, G. Bodenhausen, A. Wokaun, *Principles of Nuclear Magnetic Resonance in One and Two Dimensions*, Vol. *14*, Clarendon, Oxford **1987**.
[47] J. D. Ferry, *Viscoelastic Properties of Polymers*, 3rd ed., Wiley, New York **1980**.
[48] N. J. Inkson, R. S. Graham, T. C. B. McLeish, D. J. Groves, C. M. Fernyhough, *Macromolecules* **2006**, *39*, 4217.
[49] M. Abbasi, L. Faust, M. Wilhelm, *Adv. Mater.* **2019**, *31*, 1806484.
[50] P. Cox, E. H. Merz, *J. Polym. Sci.* **1958**, *28*, 619.
[51] W. F. Busse, *Phys. Today* **1964**, *17*, 32.
[52] S. Costa, P. F. Teixeira, J. A. Covas, L. Hilliou, *Fluids* **2019**, *4*, 66.
[53] F. J. Stadler, A. Nishioka, J. Stange, K. Koyama, H. Münstedt, *Rheol. Acta* **2007**, *46*, 1003.
[54] F. J. Stadler, C. Piel, W. Kaminsky, H. Münstedt, *Macromol. Symp.* **2006**, *236*, 209.